J. Phys. Chem. A **2010,** *114,* 2447–2463

Spectroscopic and Modeling Investigations of the Gas-Phase Chemistry and Composition in Microwave Plasma Activated $B_2H_6/Ar/H_2$ Mixtures

Jie Ma,[†] James C. Richley, David R. W. Davies, Andrew Cheesman,[‡] and Michael N. R. Ashfold*

School of Chemistry, University of Bristol, Bristol, United Kingdom, BS8 1TS and

Yuri A. Mankelevich

Skobel'tsyn Institute of Nuclear Physics, Moscow State University, Leninskie Gory, Moscow, 119991 Russia

Received: October 2, 2009; Revised Manuscript Received: December 22, 2009

This paper describes a three-pronged study of microwave (MW) activated $B_2H_6/Ar/H_2$ plasmas as a precursor to diagnosis of the $B_2H_6/CH_4/Ar/H_2$ plasmas used for the chemical vapor deposition of B-doped diamond. Absolute column densities of B atoms and BH radicals have been determined by cavity ring-down spectroscopy as a function of height (z) above a molybdenum substrate and of the plasma process conditions (B_2H_6 and Ar partial pressures, total pressure, and supplied MW power). Optical emission spectroscopy has been used to explore variations in the relative densities of electronically excited BH, H, and H_2 species as a function of the same process conditions and of time after introducing B_2H_6 into a pre-existing Ar/H_2 plasma. The experimental measurements are complemented by extensive 2-D(r, z) modeling of the plasma chemistry, which results in refinements to the existing B/H chemistry and thermochemistry and demonstrates the potentially substantial loss of gas-phase BH_x species through reaction with trace quantities of air/O_2 in the process gas mixture and heterogeneous processes occurring at the reactor wall.

1. Introduction

P-type semiconducting diamond can be formed by accommodating boron within its lattice during growth by chemical vapor deposition (CVD).[1,2] Boron incorporates at substitutional sites, creating a deep acceptor level at 0.37 eV;[3] its incorporation efficiency into CVD diamond is much higher than that of, for example, nitrogen, but its effect on growth rate and surface morphology is more variable and dependent on the growth temperature and extent of N contamination. High B dopant concentrations in the process gas mixture leads to degradation of the crystallinity and quality of the resulting diamond.[4] The most frequently used boron source gas is diborane, B_2H_6. For safety reasons, this is normally obtained as a dilute (hundreds of ppm to a few %) mixture in H_2 and used as a minor constituent in the total gas flow in a $B_2H_6/Ar/H_2/CH_4$ plasma. Many studies have sought to establish relationships between diamond film quality, dopant concentration, and plasma parameters such as the B_2H_6 flow rate (or the [B]/[C] ratio), substrate temperature, etc.[5–7] The chemistry prevailing in $B_2H_6/Ar/H_2/CH_4$ plasmas is not well established, however, and the literature contains only a handful of papers reporting diagnostics relevant to such B-containing plasmas.[8–12] Yet B-doped diamond is attracting ever growing attention, not just for its potential application in electronic and optical devices[13] but also as a result of its recently discovered superconductivity,[14–16] and potential in biosensing applications.[17,18] All such applications require reliable recipes for forming high-quality B-doped diamond with controllable doping levels, hence the emerging need for a much fuller understanding of the doping processes and the $B_2H_6/Ar/H_2/CH_4$ plasmas from which such material is grown.

Central issues relating to the gas-phase chemistry of such plasmas include the identities of the important B-containing growth species, their generation, and how their densities and distributions are influenced by discharge parameters, such as power, pressure, etc. To answer such questions through direct studies of $B_2H_6/Ar/H_2/CH_4$ plasmas is a challenge, however, given the substantial uncertainties concerning the chemistry and composition of the (simpler) $B_2H_6/Ar/H_2$ plasma. Experimental diagnosis and modeling of this latter plasma are the focus of the present paper. The additional complexities that arise upon adding CH_4 have started to be addressed by OES methods[12] and will be considered more fully in a subsequent paper.[19]

Few diagnostic studies of $B_2H_6/Ar/H_2$ plasmas have been reported. Osiac et al.[8] used optical emission spectroscopy (OES) to investigate microwave (MW) activated $B_2H_6/Ar/H_2$ plasmas at mixing ratios (3:33:64) and pressures ($p \approx 1-2$ Torr) that were, respectively, much richer in B and much lower than might typically be used in diamond CVD. These authors determined the rotational temperature of BH radicals through analysis of individual line intensities in the R branch of the $A^1\Pi \rightarrow X^1\Sigma^+(0,0)$ transition and of H_2 molecules (via the Q branch of the (2,2) band within the Fulcher-α system). Subsequent work by the same group combined OES with infrared tunable diode laser absorption spectroscopy in a more extensive investigation of MW-discharged $B_2H_6/Ar/H_2$ gas mixtures.[9] Absorptions attributable to B_2H_6, BH_3, and BH were each monitored as a function of applied power. The available spectroscopic and/or line strength data was insufficient to allow conversion of these absorption data into species densities, but the gas temperature was estimated from analysis of the rotational structure of the

---

* To whom correspondence should be addressed. Phone: (117)-9288312/3. Fax: (117)-9250612. E-mail: mike.ashfold@bris.ac.uk.

[†] Present address: Clark Hall 160, Department of Physics, Cornell University, Ithaca, New York 14850.

[‡] Present address: University of Szeged, H-6720 Szeged, Dom Ter 9, Hungary.

10.1021/jp9094694

BH(A−X) and H_2 emissions and from the Doppler broadening of individual BH absorptions. These workers also proposed a method for determining gas-phase B-atom densities based on the relative intensities of the two spin−orbit components of the 3^2S-2^2P emission at ∼250 nm. The B(^2P) densities so derived were deduced to scale less than linearly with B_2H_6 mole fraction (over the range 0−3.5%) and to account for only ∼1% of the total boron introduced in the source gas mixture.[9]

Such studies have provided new insights into $B_2H_6/Ar/H_2$ plasmas but also have their limitations. For example, OES measurements return rotational temperatures of excited-state species. Clearly, the ground-state rotational population distribution is likely to provide a better estimate of the true gas temperature, but deducing this distribution from OES data requires that a number of assumptions be made. Second, the lack of line assignments (in the case of B_2H_6) and/or line strength data (for B_2H_6, BH_3, and BH) has prevented determination of absolute densities of any of these species from the measured absorbances. Quantitative density estimates from OES measurements are fraught with difficulties. A route to determining B-atom densities from high-resolution OES data has been proposed, but the authors[9] concede that the method requires further testing in order to establish its validity. Finally, in the context of providing underpinning knowledge relevant to growth of B-doped CVD diamond, we note that these experiments involved similar MW input powers but much lower pressures ($0.75 \leq p \leq 6$ Torr) than used in most contemporary CVD reactors. This will have a number of consequences. For example, the gas temperature in the low-pressure plasmas (typically 700−1070 K) will be much lower than in the high-pressure ($p = 150$ Torr) plasmas employed in the present work, which, for BH, we show later are consistently >2000 K. The electron temperature in the low-pressure plasmas, however, will normally be much higher than in a high-pressure plasma. Both of these differences will have a major influence on the partitioning between the various B-containing species. Finally, we note that the B_2H_6 mole fraction in these low-pressure $B_2H_6/Ar/H_2$ plasmas was typically 2−3 orders of magnitude higher than that used in most B-doped CVD diamond growth.

As shown below, the presence of trace quantities of impurity (most notably air) in the process gas mixture can have very obvious effects on the boron chemistry when using low (e.g., 5−40 ppm) B_2H_6 mole fractions. Such effects map through into the resulting film properties also; both Ruan et al.[20] and Sakaguchi et al.[21] have shown how addition of small amounts of O_2 leads to a significant reduction in the extent of B incorporation into diamond films. In the context of the present work, it is appropriate to note the latter authors' suggestion[21] that the reduced B incorporation in the presence of O_2 might reflect the conversion of potential B-containing precursors into stable BO_x species through gas-phase oxidation chemistry and that there is extensive literature on the oxidation of B_yH_x species.[22,23]

Here we present the results of a combined experimental (OES and cavity ring-down spectroscopy (CRDS)) and modeling study of the gas-phase chemistry and composition in MW plasma activated $B_2H_6/Ar/H_2$ plasmas, including consideration of the effects of trace O_2 contamination (from air impurity). Such analyses, along with the results from our extensive recent study of MW activated $CH_4/Ar/H_2$ gas mixtures in this same reactor,[24–27] are necessary precursors to the detailed investigation of the gas-phase chemistry in MW activated $B_2H_6/Ar/H_2/CH_4$ mixtures (such as those used commercially for B-doped diamond growth) that will be reported elsewhere.[19] The various facets of the present study are necessarily interconnected, and we found it most straightforward to sequence the remainder of this paper as follows: After describing novel features of the experimental method (section 2), we first present background for and results of our modeling of microwave activated B/H/Ar plasmas (section 3). These provide the context but also highlight limitations in the thermochemistry and kinetics of BH_x species available in the current literature and possible (homogeneous and heterogeneous) loss processes for BH_x species. We then present the experimental measurements that have guided by, served to validate, and can be rationalized by the model predictions.

2. Experimental Section

Details of the custom-designed MW plasma-enhanced (PE) CVD reactor used in the present work have been reported previously.[25–28] Briefly, 2.45 GHz MW radiation is fed into the water-cooled aluminum-walled deposition chamber, from above, through a quartz window, creating a discharge in the Ar/H_2 gas mixture. The substrate temperature is monitored by a single-color optical pyrometer. The process gases are metered through separate, calibrated mass flow controllers (MFCs) and premixed prior to entering the reactor through two diametrically opposed 1/4 in. stainless steel pipes located close beneath the quartz window. A small amount of B_2H_6/H_2 mixture is added to the gas flow once the Ar/H_2 plasma has stabilized. Optical emission from the plasma is monitored continuously using a small monochromator equipped with a CCD detector (Oriel Instaspec IV, 600 lines mm^{-1} ruled grating) as described previously.[26] Operationally, the $B_2H_6/Ar/H_2$ plasma was assumed to have attained a stable status once the BH(A→X) emission intensity at ∼433.2 nm appeared to stop evolving, though the subsequent modeling suggests that this assumption needs reviewing (see section 3). CRDS and OES were then used to monitor the absorption and emission of selected species, simultaneously, as a function of process conditions. The experimental arrangements for spatially resolved CRDS and OES measurements have both been described previously.[25,26] In the present experiments, CRDS is used to measure both BH and B column densities (henceforth represented as {BH} and {B}), as a function of the distance (z) above the substrate while varying the applied MW power, pressure p, and flow rates $F(B_2H_6)$ and $F(Ar)$. The necessary excitation wavelengths were provided by a pulsed Nd:YAG pumped dye laser (Continuum Surelite III plus Spectra-Physics PDL-3) operating at a repetition rate of 10 Hz. The dye exalite 428 (dissolved in 1,4-dioxane) was used for measuring BH($A^1\Pi \leftarrow X^1\Sigma^+$) absorption (as in our earlier CRDS measurements of CH radicals in $CH_4/Ar/H_2$ mixtures in this same reactor.[25]) B atoms were monitored on the two $3^2S_{1/2} \leftarrow 2^2P_J$ transitions at 249.68 and 249.77 nm. The requisite wavelengths in this case were generated by frequency doubling (β-barium borate (BBO) crystal, Type-1 phase matching configuration) the output of the dye laser operating with LD 489 with subsequent beam separation using a Pellin-Broca prism. Wavelength calibration was achieved by directing a portion of the fundamental dye laser output through an etalon (free spectral range ≈ 0.85 cm^{-1}). The frequency-doubled radiation was steered by several quartz turning prisms and passed through a spatial filter prior to entering the CRDS cavity. Both sets of cavity mirrors used in this work were supplied by LayerTec Inc. and had measured reflectivities $R \approx 0.9997$ (at the relevant wavelengths for probing BH) and $R \approx 0.991$ (for the B-atom measurements).

'Base' conditions for the $B_2H_6/Ar/H_2$ plasma were chosen to be as follows: total pressure, $p = 150$ Torr; input power, $P =$

TABLE 1: Kinetic Parameters for Likely Reactions Occurring in a B/H Gas Mixture Together with Likely B/H/O Coupling Reactions in the Presence of Trace O_2 Impurity[a]

	reactions	A/cm^3 mol^{-1} s^{-1}	B	(E/R)/K	ref
$R1$	$B_2H_6 + B_2H_6 \leftrightarrow BH_3 + BH_3 + B_2H_6$	2.5×10^{17}	0	17 008	[b]
$R2$	$BH_3 + H \leftrightarrow BH_2 + H_2$	4.8×10^{11}	0.69	1211	10
$R3$	$BH_2 + H \leftrightarrow BH + H_2$	1.44×10^{12}	0.69	1211	10
$R4$	$BH + H \leftrightarrow B + H_2$	1.44×10^{12}	0.69	1211	10
$R5$	$B_2H_6 + BH_3 \leftrightarrow B_3H_7 + H_2$	1.65×10^{13}	0	4378	[b]
$R6$	$B_3H_7 + B_2H_6 \rightarrow B_4H_{10} + BH_3$	1.76×10^{17}	0	10 396	[b]
$R7$	$B + H_2O \rightarrow HBO + H$	2.4×10^{14}	0	1349	41, 53
$R8$	$B + O_2 \leftrightarrow BO + O$	7.24×10^{13}	0	156	41
$R9$	$B + OH \leftrightarrow BO + H$	6.0×10^{13}	0	0	41
$R10$	$BH + H_2O \leftrightarrow HBO + H_2$	3.0×10^{12}	0	191	23
$R11$	$BH + O_2 \leftrightarrow HBO + O$	2.95×10^{13}	0	1207	23
$R12$	$BH_2 + O \leftrightarrow BO + H_2$	5.0×10^{13}	0	0	23
$R13$	$BH_2 + O_2 \leftrightarrow HBO + OH$	10^{10}	0	0	23
$R14$	$BH_3 + H_2O\ (O_2) \rightarrow$ products	$<3 \times 10^9$	0	0	23

[a] Rate constants are expressed in the traditional form $k[\text{cm}^3\ \text{mol}^{-1}\ \text{s}^{-1}] = f(A, B, T) = AT^B \exp(-E/RT)$. [b] Present study.

1.5 kW; flow rates $F(\text{Ar}) = 40$ standard cm^3/min (sccm), $F(H_2) = 525$ sccm. The B_2H_6 source gas used in most of the experiments was specified as 200 ppm in H_2, though some of the time-dependent studies of BH(A → X) OES employed a more concentrated gas mixture (5% B_2H_6 in H_2). Two factors (the different absolute transition strengths and the different mirror reflectivities) necessitated the use of different B_2H_6 flow rates for the B and BH measurements. Once $F(B_2H_6) > 0.005$ sccm (i.e., if the flow rate of the 200 ppm B_2H_6 in H_2 source gas was >25 sccm), the measured B absorption signal clearly started to saturate (i.e., the ring-down time constant became too short to measure reliably with the available mirrors, cavity length, dye laser pulse duration, and collection electronics), even when monitoring the weaker of the two absorption lines (the $3^2S_{1/2} \leftarrow 2^2P_{1/2}$ transition). Saturation results in an underestimation of the true B column density. Unfortunately, the BH absorption is too weak to measure reliably at such low $F(B_2H_6)$ values. In what follows, therefore, base conditions for BH column density measurements are defined as $F(B_2H_6) = 0.009$ sccm, while for B-atom measurements we choose $F(B_2H_6) = 0.003$ sccm as the base condition. As in our recent diagnoses of $CH_4/Ar/H_2$ mixtures in this same reactor,[25–27] when varying one discharge parameter, all others were maintained at their base values except when investigating the effects of varying $F(\text{Ar})$ and/or $F(B_2H_6)$, where any variation away from the base condition was compensated by adjusting $F(H_2)$ so as to ensure that $F_{\text{total}} = 565$ sccm.

3. 2-D Modeling of B/H/Ar Chemistry in MW PECVD Reactors

3.1. 2-D Model of MW Discharge Processes. The 2-D model used to describe the essential processes occurring in the present MW PECVD reactor and to provide spatial distributions of the gas temperature, T_{gas}, and species concentrations, power absorption and transfer channels as a function of reactor operating conditions has been described previously.[24] Briefly, the model assumes cylindrical symmetry with coordinates r (the radial distance from the center line of the chamber) and z (the axial (vertical) height above the substrate surface), a reactor radius $R_r = 6$ cm, and height $h = 6$ cm. MW power absorption and the activation volume are incorporated as parameters within the model, thereby allowing estimation of the reduced electric field (E/N) and the electron temperature (T_e) in the plasma region for any given value of P. The main model blocks are incorporated in a self-consistent manner and describe the following: (i) power absorption and gas heating, heat and mass transfer; (ii) plasma activation of the reactive gas mixture, plasma-chemical kinetics, and involve nonequilibrium electron energy distribution function (EEDF) calculations and species diffusion and thermal diffusion; and (iii) gas−surface processes (deposition and the loss/production of radicals, ions, and electrons). The set of nonstationary conservation equations for mass, momentum, energy, and species concentrations are solved numerically by a finite difference method in (r, z) coordinates.

The 2-D model takes into account the changes in plasma parameters and conditions (e.g., T_e, T_{gas}, electron concentrations (n_e), power density (Q), and the plasma chemistry) as a result of variations in reactor parameters (p, P, and the mole fractions of B_2H_6, Ar, etc., in the input gas mixture). This model procedure, which uses the plasma size as an external parameter, has been described in detail elsewhere.[24] Our previous studies of MW activated C/H/Ar gas mixtures employed a base plasma chemical mechanism involving 38 species and >240 reactions,[24] which we have now supplemented with two additional blocks describing reactions involving B_yH_x species and H_xO_z species. The latter allows study of the effects of trace amounts of air contaminant on boron species. The present paper focuses on B/H/Ar plasmas; thus, for the present analysis all reactions involving carbon-containing species were switched off.

3.2. B/H Gas-Phase Chemistry and Thermochemistry. The available thermodynamic and kinetic data for B/H/Ar gas mixtures is surprisingly sparse and variable. As done previously,[11] we start with the minimalist reaction mechanism $R1$−$R4$ in Table 1 to describe the interconversion between the various BH_x species. Table 2 summarizes some of the available thermochemical data for these reactions and for B_yH_x species[29–34] along with the results of additional ab initio calculations performed as part of the present study. The latter were calculated at the B3LYP/6-311G** level of theory and vibrational frequencies calculated so as to provide zero-point (and 298 K) energies.

As Table 2 shows, there is reasonable consensus relating to the endoergicity of $R1$ and the exoergicity of $R4$, but the $\Delta_f H^\circ$ values for $R2$ and $R3$ derived using the NIST-JANAF compilation[30] are very different from most other recent estimations, all of which suggest that $R2$ is mildly endothermic and that the exothermicity of $R3$ is comparable to that of $R4$. As shown by Rayar et al.,[12] such $\Delta_f H^\circ$ values ensure that the equilibrium constant for $R2$ is only weakly temperature dependent in the range $1500 \le T_{\text{gas}} \le 3000$ K relevant to the present studies, whereas those for $R3$ and $R4$ are large and positive but decline with increasing T_{gas}. The present ab initio calculations confirm previous findings[34] that $R2$ and $R4$ show modest energy barriers

TABLE 2: Compilation of Published Thermochemical Data for the B-Containing Reactions *R*1−*R*4 in a B_2H_6/Ar/H_2 Plasma and for the Various B_yH_x Species Implicated in the Present Work[a]

	$\Delta_rH°$ (298 K)/kJ mol^{-1}						
reaction	ref 30	ref 31	ref 33	ref 32	ref 34[b]	ab initio[c]	adopted value
*R*1	172.4	142.0	163.8	139.4		124	141.6
*R*2	−123.8	10.8		12.3	2.9	13.2	8
*R*3	23.9	−93.3		−93.6		−92.8	−93
*R*4	−100.7	−100.0		−95.7	−89.9	−89.9	−96

	$\Delta_fH°$ (298 K)/kJ mol^{-1}			
species	ref 30	ref 29	ref 31	adopted value
B	560 ± 12	565	560 ± 12	565
BH	442.7 ± 8.4	446	442.7	443
BH_2	201 ± 63	295	318.0	318
BH_3	106.7 ± 10	92	89.2	92
B_2H_6	41 ± 16.7	37	36.4	42.6
B_3H_7			128.4	128.4
B_4H_{10}			66.1	66.1

[a] Values adopted in the present study are listed in the final column. [b] Zero-point values calculated at the G2 level of theory. [c] Zero-point values calculated in the present work at the B3LYP/6-311G** level of theory.

in the forward direction. We were unable to locate a transition state for the abstraction *R*3 and conclude that this reaction proceeds via an addition/elimination mechanism. Such expectations accord with the previous work of Schlegel et al.,[34] who argue that *R*2 will also proceed via such a mechanism at lower temperatures. Analysis of the available thermochemical data and the present calculated data leads to a set of enthalpies $H(T)$, heat capacities $C_p(T)$, and entropies $S(T)$ that (apart from BH_2) are largely consistent with the values reported by Glushko,[29] the JANAF recommendations,[30] and other recent data.

Table 1 lists the parameters used in the present modeling of the rate constants k_i ($i = 1-4$) expressed in the traditional form $k = f(A, B, T) = AT^B \exp(-E/RT)$. The initial production of BH_x species is determined by the rate of B_2H_6 decomposition. Both the rate and the order of the diborane thermolysis reaction[35,36] have been matters of long-standing controversy however. Clarke and Pease[35] showed that the rate of diborane decomposition increased over the gas temperature range $358 < T_{gas} < 436$ K and was depressed by addition of H_2 but unaffected by the presence of N_2 or by an increase in reactor surface area. We attempted to simulate these data in order to determine k_1, which is not well known (particularly at higher temperatures), by adopting a reduced version of the previously proposed mechanism[35] that includes *R*1 (with M = B_2H_6), *R*5, and *R*6 in Table 1 involving reactive intermediates BH_3 and B_3H_7[36] and the thermochemical data listed in Table 2.

To accommodate reaction pathways to the higher order boranes (B_5H_{11}, B_5H_9, $B_{10}H_{14}$, B_4H_{10}, etc.) detected experimentally[36] along with H_2, we excluded the reverse reaction *R*−6 from the mechanism *R*1−*R*6 and assumed that the subsequent chemistry involving such higher boranes does not impact seriously on the initial stages of diborane thermolysis. Reactions $i = 1$, 5, and 6, with the adopted rate coefficients $k_i(T)$ listed in Table 1 result in saturation of $[BH_3]$ and $[B_3H_7]$ in the early stages of thermolysis and satisfactorily replicate the 3/2 power dependence of the B_2H_6 loss rate ($R_{loss} \approx 2(k_{-1}/k_1)^{0.5}k_2[B_2H_6]^{1.5}$) and the H_2-induced inhibition observed experimentally. The activation energy E_1 was taken as the reaction enthalpy, while the E_i ($i = 5, 6$) values for *R*5 and *R*6 were chosen so as to reproduce the experimentally observed temperature dependence of B_2H_6 loss: $R_{loss} \approx \exp(-12880/T)$. Given these temperature dependences, the pre-exponential factor A_1 must be confined to lie within a narrow range. A_1 has to be $>2.5 \times 10^{17}$ cm^3 mol^{-1} s^{-1} to provide the minimal BH_3 production rates consistent with the early time measurements of Clarke and Pease,[35] but at the highest temperatures relevant to the present work ($T \approx 2900$ K) we require $A_1 < 2 \times 10^{17}$ cm^3 mol^{-1} s^{-1} in order that k_1 is within the gas kinetic collision limit: $k_1 < 6 \times 10^{14}$ cm^3 mol^{-1} s^{-1}.

Serial calculations were thus run with $A_1 = 2.5 \times 10^{17}$ cm^3 mol^{-1} s^{-1}. We note that significant variations of A_1 and/or $E_{a,1}$ (e.g., $k_1 = 4.3 \times 10^{17} \exp(-14\,942/T)$) resulted in relatively minor variations in the calculated $\{BH_x\}$ (less than a factor of 2) and in the r value (a few millimeters only) of the annular region at which the B_2H_6 dissociation rates are maximal, i.e., variations of k_1 (via changes in A_1 and/or $E_{a,1}$) do not have a large effect the calculated profiles or absolute number densities of the various BH_x species. We also explored possible contributions to B_2H_6 dissociation via collisions with other partners M (e.g., M = H_2 rather than M = B_2H_6), which are not included in the present reaction mechanism. We have no direct data regarding B_2H_6 dissociation promoted by collisions with H_2 (the most abundant species under the present reactor conditions) at high temperatures, but indirect data[11,37] suggests that the enhancement factor with H_2 as a collision partner should be much lower than with B_2H_6, i.e., $A_1(M = H_2) < 10^{-4} \times A_1(M = B_2H_6)$. Further 2-D model calculations with M = H_2 in *R*1 indicate that this condition may be yet more stringent: calculations assuming $A_1(M = H_2) > 10^{-5} \times A_1(M = B_2H_6)$ yield results that are inconsistent with the CRDS data reported in section 4. The present 2-D calculations thus assume that *R*1 involves M = B_2H_6 only, with associated rate coefficient $k_1(T)$, across the whole temperature range $300 \text{ K} < T < 3000$ K. M = H_2 or any other collision partners may redistribute the spatial profiles of the B_2H_6 dissociation rate (i.e., of the primary BH_x radical source). The aggregate value of this source is weakly dependent on k_1 however. In all cases, most of the B_2H_6 molecules that diffuse from the cool, near-wall regions into the hot plasma region are decomposed (the calculated diborane mole fraction, X_{B2H6}, in the hot plasma core is only ∼1% of the initial X^0_{B2H6} in the input source gas). The BH_x source is limited by diffusional transfer of B_2H_6 and is thus predicted to show a first-order dependence on X^0_{B2H6}, in accord with the CRDS and OES measurements of BH_x species reported in sections 4.1.3 and 4.2.2.

Our initial 2-D model calculations resulted in the typical diffusional profile of B_2H_6 concentration (increasing with distance from the plasma center (as in Figure 1). However, this preliminary modeling based simply on $R1-R4$ predicts {B} and {BH} values that are both significantly higher (by more than an order of magnitude) than the column densities measured by CRDS (see section 4.1). Moreover, we recognize that the minimalist scheme $R1-R4$ is likely to underestimate the concentrations of B, BH, etc. species since we do not allow for possible contributions from H-shifting reactions of the form

$$B_2H_x + H \leftrightarrow B_2H_{x-1} + H_2 \quad (x \le 6)$$

and subsequent decay of B_2H_{x-1} species as a route to forming BH_x species. Part of this discrepancy is likely to be attributable to the approximate B/H reaction scheme employed (for example, we do not include possible formation of heavier B_yH_x ($y > 2$) species in the cool periphery of the reactor) and to continuing uncertainties in the reaction rate coefficients. Varying the rate coefficients (k_2, k_3, and k_4) of the fast H-shifting reactions $R2-R4$ has little effect on the calculated results, however, since these reactions are (largely) in equilibrium with the corresponding reverse reactions. The partitioning of the BH_x species is thus determined largely by their thermochemical properties. It seems improbable that these uncertainties, or uncertainties in the primary source of BH_3 radicals (i.e., B_2H_6 dissociation balanced by diffusion of diborane from the cool periphery), could result in such a serious overestimation of the BH_x species densities. Thus, we are forced to consider (and attempt to quantify) other possible loss processes for BH_x species. The present measurements suggest a need to include two additional factors in any more realistic modeling of such $B_2H_6/Ar/H_2$ plasmas: loss of boron to the reactor walls and unintended B/H/O chemistry induced by trace air (O_2) impurity in the process gas mixture. These effects are now considered in turn in sections 3.3 and 3.4.

3.3. Heterogeneous Loss of BH_x Species. Even with a well-passivated gas delivery line, the OES measurements shown in section 4.2.3 reveal a significant (~15 min) induction period between activating the B_2H_6 (in H_2) gas flow into a pre-existing Ar/H_2 plasma and discernible BH radical emission from the plasma region. Comparing the estimated number of B atoms supplied to the reactor during this time (in the form of B_2H_6) and the number of surface sites on the reactor wall leads to the conclusion that $\geq 1\%$ of the input B would need to accumulate on the reactor wall in order to achieve a complete monolayer coverage in ~15 min. The material deposition studies reported in section 4.3 indicate that loss to the side walls continues after that time, leading, eventually, to the build up of macroscopic quantities of nanostructured material. Estimation of the total amount of boron in the deposited material suggests that only a small fraction (a few percent) of the input boron density is incorporated into the material deposited on the reactor side wall however.

We simulated a continuous boron loss at the reactor walls and substrate surface as fluxes $F_x = \gamma[BH_x]\upsilon_T/4$, where γ is the loss probability of BH_x ($x = 0-3$) species, $[BH_x]$ represents the concentrations of these species near the wall, and υ_T is the thermal velocity of such species. These calculations indicate that the main effect of such losses is to reduce $[BH_x]$ in the entire reactor volume with the most dramatic declines in the cold, near-surface regions. Calculations assuming two different loss probabilities, $\gamma = 0.1$ and 1, yield very similar fluxes. For example, the sum of the fluxes ΣF_x at the point $z = 0.95$ cm, $r = R_r = 6$ cm is $\sim 2 \times 10^{12}$ cm^{-2} s^{-1} in both cases, with B atoms providing the dominant contribution. The total loss of BH_x per second can thus be calculated as the integral over the total surface area $\int(\Sigma F_x)\,dS \approx 2 \times 10^{15}$ s^{-1}, which is ~25% of the rate at which boron enters the reactor ($2 \times F(B_2H_6) \equiv 8 \times 10^{15}$ B atoms s^{-1} for $F(B_2H_6) = 0.009$ sccm). The calculations suggest different BH_x fluxes incident at different locations within the reactor, i.e., ~22% of the total flux on the substrate and substrate holder, ~63% on the bottom surface of the reactor, ~12% on the side walls (at $r = R_r = 6$ cm), and ~3.5% on the top quartz window. The calculated flux incident on the reactor side walls is reassuringly consistent with experimental estimates of the amount of deposited boron, but this accounts for only ~3% of the B atoms introduced into the reactor in the form of B_2H_6. As shown later (section 4.2.3), the experimental measurements indicate some etching of boron-containing material from the reactor wall. Thus, the net deposition rate will be less that the 25% estimated above (i.e., $<2 \times 10^{15}$ s^{-1}). Further, the foregoing estimates of the relative contributions from the different surfaces to the net deposition rate include no allowance for local variations in surface material (e.g., aluminum, molybdenum, quartz) and conditions (e.g., different etching and deposition rates from the hot substrate holder and the cold side wall) which could affect the calculated relative contributions of the different surfaces.

Another factor, of potentially greater importance, is that B_yH_x species can react heterogeneously with surface-adsorbed H_xO_z species or be adsorbed at the surface and then react with H_xO_z species. As shown later (section 4.3), postdeposition analysis shows material deposition on the reactor walls and that this material contains O as well as B and H. This O content could also arise via reaction with an oxide coating or with adsorbed H_2O on the reactor wall during deposition. The deposited material appears to be hygroscopic; visually it looks moist. A more detailed discussion of the possible gas−surface chemistry by which such material is formed is reserved until section 4.3. Temporal studies of BH* emission intensities (section 4.2.3) suggest that much of this deposition may occur during the initial stages of surface treatment (i.e., before the B_2H_6 concentrations and BH* emission intensities attain their steady-state values). None of the foregoing theoretical analyses nor the experimental measurements reported in section 4.2 indicate that heterogeneous loss processes could seriously affect the absolute concentrations of the various gas-phase B_yH_x species in the plasma region under steady-state conditions however. Some other permanent loss process must therefore be operating within the reactor. Since we see clear evidence of BH depletion when the process gas mixture contains trace quantities of air impurity (section 4.2.4), we now consider the possible effect of air (oxygen) contamination within the frame of a B/H/O gas-phase chemical mechanism.

3.4. B/H/O Gas-Phase Chemistry. The direct and reproducible OES measurements (see section 4.2.4) suggest that traces of air impurity initiate chemistry that removes BH_x species from the gas phase. Thermal dissociation of N_2 at the prevailing gas temperatures will be negligible, and 0-D calculations suggest that electron impact induced dissociation of N_2 (and subsequent H-shifting reactions) will result in steady-state NH_x species concentrations $< 10^{10}$ cm^{-3}. Thus, we ignore the possible effects of N/B coupling reactions. O_2 is a different matter altogether. B, BH, and BH_2 radicals each react efficiently with O_2, H_2O, and other H_xO_z species,[23] binding boron into various stable $H_xB_yO_z$ species which, for simplicity, we assume to be HBO in the reduced chemical mechanism $R7-R14$ which has been

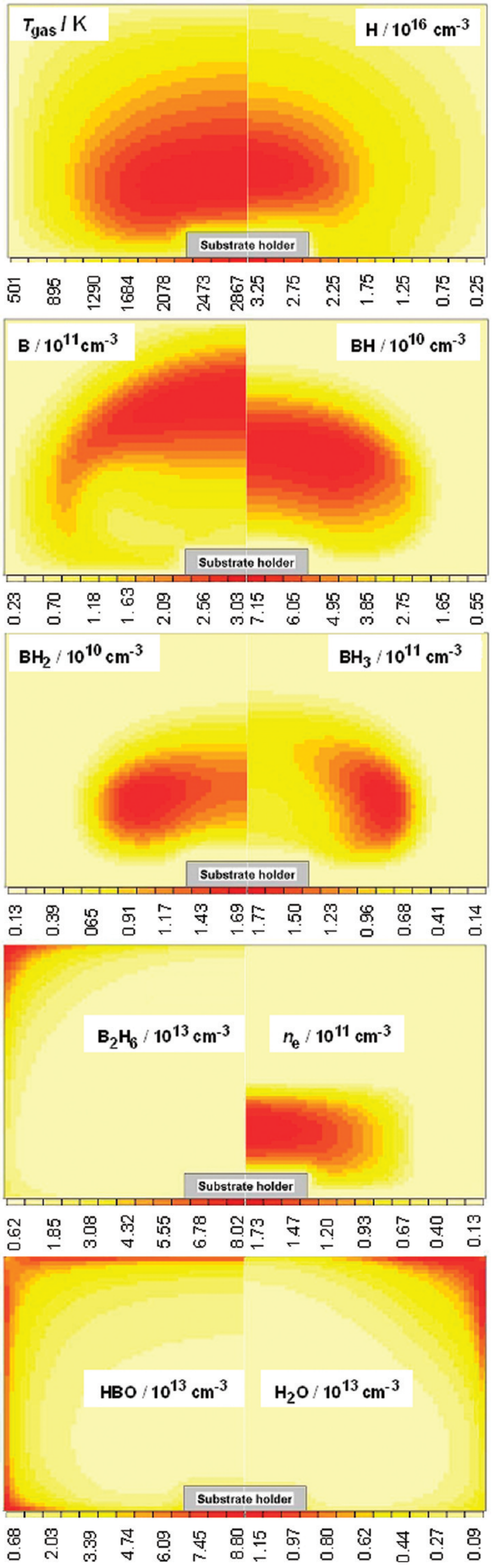

Figure 1. 2-D(r, z) false color plots showing the calculated distributions of T_{gas} and number densities of H, B, BH, BH_2, BH_3, B_2H_6, electrons, HBO, and H_2O based on the thermochemistry and reaction mechanism listed in Tables 1 and 2 under base conditions, i.e., $P = 1.5$ kW, $p = 150$ Torr, $F(H_2) = 525$ sccm, $F(Ar) = 40$ sccm, $F(B_2H_6) = 0.009$ sccm, and $F(O_2) = 0.006$ sccm.

incorporated in the model chemistry block (Table 1). O_2 molecules only survive in the cold regions within the reactor, e.g., near the gas inlet ports. In the hot plasma regions, the presence of H atoms and molecular H_2 ensures conversion of O_2 to H_2O (via reactive intermediates like O and OH). An H/O chemical mechanism[38] has thus been added to the model chemistry block in order to accommodate these temperature-dependent conversion processes and derive spatial profiles for the various H_xO_z species.

A minimal estimate of the extent of any air contamination leaking into the reactor during operation was obtained as follows. The valve to the rotary pump was closed and the time taken for the pressure, p, in the reactor to rise to a certain value was measured and compared with that taken to achieve the same p when flowing 1 sccm CH_4 through a MFC that had been calibrated by companion quantum cascade laser absorption measurements.[27] The air leak determined by this method corresponded to a flow rate of ~0.028 sccm (i.e., ~0.006 sccm of O_2). This estimation of $F(O_2)$, which corresponds to ~10 ppm of the total gas flow and is thus comparable with the B_2H_6 flow rates used in this work ($0.003 \leq F(B_2H_6) \leq 0.024$ sccm), includes no allowance for any air impurity in any of the source gases. Nonetheless, 10 ppm of O_2 is sufficient to have a significant impact on the gas-phase BH_x concentrations. The present 2-D calculations for a B/H/Ar plasma in the presence of trace amounts of O_2 identify reaction of B atoms with H_2O ($R7$)) as the most important BH_x loss process. Other BH_x ($x > 0$) species are depleted indirectly; the fast H-shifting reactions $R2$—$R4$ allow efficient redistribution of population among these species to extents that depend on the local T_{gas} and H atom to H_2 concentration ratio, i.e., $[BH_x]/\Sigma[BH_x] = f_x(T_{gas}, [H]/[H_2])$. The forward and reverse rates (R_i and R_{-i}, $i = 2-4$) of these H-shifting reactions are in local equilibrium (i.e., $R_i \approx R_{-i}$) and at least 3 orders of magnitude faster ($R_i \approx 10^{17}-10^{18}$ cm^{-3} s^{-1} in the hot plasma region) than the net rates ($R \approx 10^{12}-10^{14}$ cm^{-3} s^{-1}) of BH_x production (mainly by reaction $R1$) and loss (by $R7$).

The important B/O coupling reaction $R7$ ensures that HBO is one of the dominant B/O-containing products throughout most of the reactor volume. Ab initio calculations highlight the multistep nature of the B + H_2O reaction, which involves multiple pathways, transition states, and products (e.g., BOH + H, *trans*- and *cis*-HBOH, BO + H_2, etc.).[39,40] The concentrations of these various boron-containing products will all be much lower than that of the more stable HBO species, and these alternative products are not treated in the model. We also neglect the reverse transfer HBO + H → B + H_2O ($R-7$) because of its high (but poorly defined) energy barrier and the paucity of detail regarding this complex transition. The reverse reaction $R-7$ as parametrized by Yetter et al.[41] and Pasternack[42] could seriously overestimate the true rate of the HBO + H reaction. Further model calculations, including $R-7$, show HBO destruction in the hot plasma region and consequently increased B and BH column densities that deviate further from the CRDS measurements reported in section 4.2.

3.5. 2-D Model Results and Species Distributions.

Having added blocks to describe B/H/O chemistry and possible BH_x surface losses, the 2-D model was then used to study the various processes in a B/H/O/Ar plasma operating in the Bristol MW PECVD reactor and enable comparison between model and experimental results. In what follows, the model outputs are mainly presented for base conditions, defined as follows: total pressure, $p = 150$ Torr; input power, $P = 1.5$ kW; total flow rate, $F_{total} = 565$ sccm of a gas mixture comprising 0.0016%B_2H_6/

0.001%O_2/7%Ar/balance H_2. Calculations were also carried out with $F(B_2H_6) = 0.003$ sccm in order to allow direct comparison with the experimental measurements of {B}. For the base conditions and plasma sizes (plasma radius $r_{pl} \approx 3.65$ cm and height $h_{pl} \approx 1.9$ cm), the 2-D model returns the following typical parameter values in the plasma core: $T_e \approx 1.23$ eV, average power density $Q \approx 18$ W cm^{-3}, maximal $T_{gas} \approx 2870$ K, H-atom mole fraction, $X_H \approx 0.064$ and concentration [H] $\approx 3.25 \times 10^{16}$ cm^{-3}, and electron concentration $n_e \approx 1.7 \times 10^{11}$ cm^{-3}. The 15% increase in the plasma volume as compared with a pure 7% Ar in H_2 plasma operating under these same conditions (for which $r_{pl} \approx 3.5$ cm and $h_{pl} \approx 1.8$ cm) leads to the following notable reductions in column density of selected species at $z =$ 9.5 mm: ~9% for electrons, ~15% for H_2*, and ~20% for H ($n = 2$ and 3) and Ar**. Much smaller reductions are calculated for H ($n = 1$) (~0.5%), the maximum T_{gas} (0.5%), and T_e (2.3%). The expansion in plasma volume upon adding even trace amounts of B_2H_6 is most probably the result of additional ionization of BH_x species, at lower T_e, in the outer regions of the plasma, reflecting their low ionization potentials (I(B) $\approx$ 8.3 eV, I(BH) $\approx$ I(BH_2) $\approx$ 9.8 eV), and serves to explain (in part at least) the observed drop in H_2*, H_α, and H_β emission intensities (section 4.2.2) and the decline in substrate temperature.

Figure 1 shows 2-D(r,z) false color plots of the calculated T_{gas} and H, B, BH, BH_2, BH_3, B_2H_6, electrons, HBO, and H_2O number density distributions for the base conditions (with the radial, r, axis directed horizontally and the axial z axis directed vertically and ($r = 0$, $z = 0$) defining the center of the substrate surface). These serve to illustrate the progressive conversion of B_2H_6 to BH_3 and then to the smaller BH_x species with increasing T_{gas}, but contrary to earlier assumptions,[12] the present modeling also suggests that the B_2H_6 concentrations in the hot plasma region are comparable with those of the smaller BH_x species. The plasma-chemical modeling predicts that the various BH_x species concentrations all maximize outside the hottest region and that the [BH_x] distributions extend over much wider regions of r, z space than, for example, the [C_2] and [CH] distributions in CH_4/Ar/H_2 plasmas operating in this same reactor at the same P and p conditions.[24,25] These findings reflect the primary source of the BH_x species (diffusion of diborane from the cold regions of the reactor and subsequent B_2H_6 dissociation) and the lower temperatures required to drive the H-shifting reactions $R2$—$R4$. Such predictions are in good qualitative accord with the z-dependent {B} and {BH} profiles measured by CRDS and the mean rotational temperature derived from analysis of the BH(A—X) absorption line intensities, reported in section 4.1. The predictions are also consistent with previous measurements and modeling of B-atom densities in hot filament activated B_2H_6/H_2 gas mixtures,[11] wherein B_2H_6 dissociation (therein described by $R1$ with M = H_2) fits satisfactorily with the dissociation rate (with M = B_2H_6) used here.

Figure 2 shows the radial (r) distributions of T_{gas} and the concentrations of various boron species calculated for $z = 9.5$ mm for two different $F(B_2H_6)$ values: (a) the oxygen-deficient regime ($F(B_2H_6) > F(O_2)$, $F(B_2H_6) = 0.009$ sccm) and (b) the boron-deficient regime ($F(B_2H_6) < F(O_2)$, $F(B_2H_6) = 0.003$ sccm). Concentration profiles for O_2, H_2O, and OH are included also. The calculated 'effective' rotational temperature of the BH radicals under the former base conditions (i.e., the density-weighted temperature, averaged over the entire viewing column), $T_{rot} \approx 2530$ K, is indicated in Figure 2a, cf. the experimentally determined value $T_{rot} \approx 2300$ K. More detailed comparisons of the model predictions and experimental column density measurements are reserved until section 4.

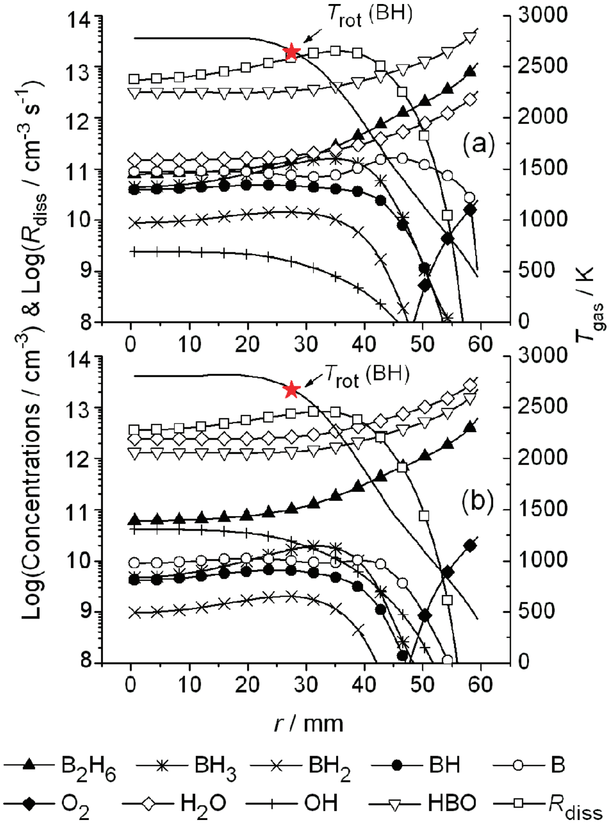

Figure 2. Radial distributions of T_{gas} (right-hand axis), the B, BH, BH_2, BH_3, B_2H_6, HBO, H_2O, O_2, and OH concentrations (in cm^{-3}, left-hand axis), and the B_2H_6 dissociation rate R_{diss} (in cm^{-3} s^{-1}, left-hand axis) calculated at $z = 9.5$ mm for (a) $F(B_2H_6) = 0.009$ sccm and (b) $F(B_2H_6) = 0.003$ sccm assuming the same level of O_2 impurity (10 ppm) as used in the false color plots shown in Figure 1.

Under base conditions, the calculated HBO concentrations in the plasma core are >3 × 10^{12} cm^{-3} and more than 1 order of magnitude higher than the concentrations of other B_yH_x species, as shown in Figure 2a. HBO production is limited by the available oxygen species (H_2O) when $F(B_2H_6) > F(O_2)$ (Figure 2a) and when $F(B_2H_6) < F(O_2)$ by the available BH_x species (Figure 2b). A noticeable change in the variation of [BH_x] with $F(B_2H_6)$ can be anticipated when $F(B_2H_6) \approx F(O_2)$. Once $F(B_2H_6) > F(O_2)$, BH_x conversion to the HBO reservoir species is suppressed (owing to depletion of the available H_2O) and the various BH_x concentrations are predicted to increase more steeply and near linearly with $F(B_2H_6)$. Such a trend, which is clearly seen for both {B} and {BH} by CRDS (section 4.1) and for [BH] by OES (section 4.2), provides another route to estimating O_2 impurity levels in the process gas by considering the balance between the total boron (X_{total}(B)) and oxygen (X_{total}(O)) species. The BH concentration can be expressed as

$$[BH] = (\Sigma X_{BHx})Nf_1 = (X_{total,B} - 2X_{B2H6} - X_{HBO})Nf_1$$

where N is the gas concentration and X_{ByHx} is the B_yH_x mole fraction. Under base conditions (i.e., $F(B_2H_6) > F(O_2)$), HBO is the main oxygen-containing species in and around the plasma (i.e., in the region where BH is most abundant), as shown in Figure 2a. Thus, in the same way that X_{total}(B) is related to $F(B_2H_6)$, X(HBO) will scale with $F(O_2)$, and given $X_{total}(B) \gg X(B_2H_6)$, as is the case in the plasma region (Figure 2a), the above analysis implies that when $F(B_2H_6) > F(O_2)$ the concentrations of BH (and electronically excited BH*) are given by

$$[\mathrm{BH}] \sim [\mathrm{BH}^*] \sim (F(\mathrm{B_2H_6}) - F(\mathrm{O_2}))$$

In the boron-deficient regime ($F(B_2H_6) < F(O_2)$), [B] and [BH] fall steeply with decreasing $F(B_2H_6)$, as can be seen by comparing Figure 2a and 2b. BH signals measured by both CRDS and OES (Figures 4a and 6a below) accord with these model predictions: both appear to cut off at $F(B_2H_6) \approx 0.006$ sccm, consistent with the $F(O_2)$ impurity leak rate assumed in all of the present modeling. As noted previously, calculations with $F(O_2) = 0$ return B and BH column densities that are typically an order of a magnitude higher than those calculated with $F(O_2) = 0.006$ sccm and those measured by CRDS (see section 4.1).

4. Experimental Results and Discussion

Adding trace amounts of B_2H_6 to a pre-existing Ar/H_2 plasma has two very noticeable effects. First, the luminous plasma region visibly expands and changes color, from pale pink to purple. Second, the substrate temperature declines from, in the present case, ~1050 K when operating with the pure 7% Ar in H_2 plasma under base conditions to ~985 K when $F(B_2H_6) = 0.01$ sccm.

4.1. CRDS Measurements and Results. ***4.1.1. Spectra.*** Figure 3 shows typical absorption spectra of the spin−orbit split $3^2S_{1/2} \leftarrow 2^2P_J$ transition of atomic boron and selected R branch lines within the BH(A ← X) (0,0) band measured by CRDS. All of these absorptions are well described by Gaussian line shapes, as expected given the dominance of Doppler broadening to the overall line width. The measured $B(3^2S_{1/2} \leftarrow 2^2P_{3/2})$ absorption displayed in Figure 3a is about twice that of the $B(3^2S_{1/2} \leftarrow 2^2P_{1/2})$ line. The intrinsic absorption cross sections of the two transitions are very similar. The different absorbances can be traced to the fact that the wavenumber separation between the $2^2P_{3/2}$ and the $2^2P_{1/2}$ levels is only ~15 cm^{-1} (~22 K), as shown in the inset to Figure 3a. Since $T_{\rm gas}$ in the plasma volume under typical experimental conditions is >2000 K, the relative populations of the $2^2P_{3/2}$ and $2^2P_{1/2}$ levels are determined by their respective degeneracies, viz. 2:1. Given the comparatively low reflectivity of the CRDS mirrors available for measurements at ~249 nm, even relatively small absorbances can reduce the ring-down time to the extent that the decay constant can no longer be measured accurately, resulting in an apparent 'saturation' of the absorption peak. The 2:1 ratio provides a convenient criterion for judging the extent to which any B absorption measurements are affected by such saturation effects. Inspection of Figure 3b and 3c shows that each 'line' in the BH(A−X) spectrum appears with a weaker satellite line. The strong and weak lines in each case are associated with, respectively, the ^{11}BH and ^{10}BH isotopologues. The line intensities should reflect the respective natural abundances (4:1); this ratio also serves as a criterion when judging if a measured ^{11}BH absorption has started to become saturated at high $F(B_2H_6)$.

4.1.2. Temperature and Column Density Determinations. The relative intensities of the rotational lines in Figure 3b allow estimation of an effective rotational temperature of the ground-state BH radicals ($T^X_{\rm rot}$). Given the high operating pressures ($p = 150$ Torr) and thus high collision frequencies, rotational (R)−translational (T) energy transfer is efficient and $T^X_{\rm rot}$ provides a good estimate of $T_{\rm gas}$ in the region in which the BH radicals are localized.

Rayar et al.[10] presented a detailed description of the procedure for extracting rotational temperatures from BH(A−X) spectra recorded in emission. The analysis for spectra recorded in absorption is very similar[43] and, in the case of the A ← X (0,0) R branch lines shown in Figure 3b, leads to the final expression

$$-\ln\left(\frac{I_{J'\leftarrow J''}}{J'+1}\right) \propto \frac{E_{J''}}{T^X_{\rm rot}} \tag{1}$$

where J'' and J' are the rotational quantum numbers in, respectively, the lower and upper states, $E_{J''}$ is the rotational energy of a BH(X)$_{v=0,J''}$ radical, and $I_{J'\leftarrow J''}$ is the measured line absorbance. A plot of the $\ln((I_{J'\leftarrow J''})/(J'+1))$ measured in a B_2H_6/H_2/Ar plasma operating at base conditions against $E_{J''}$ (calculated using the spectral simulation program PGO-

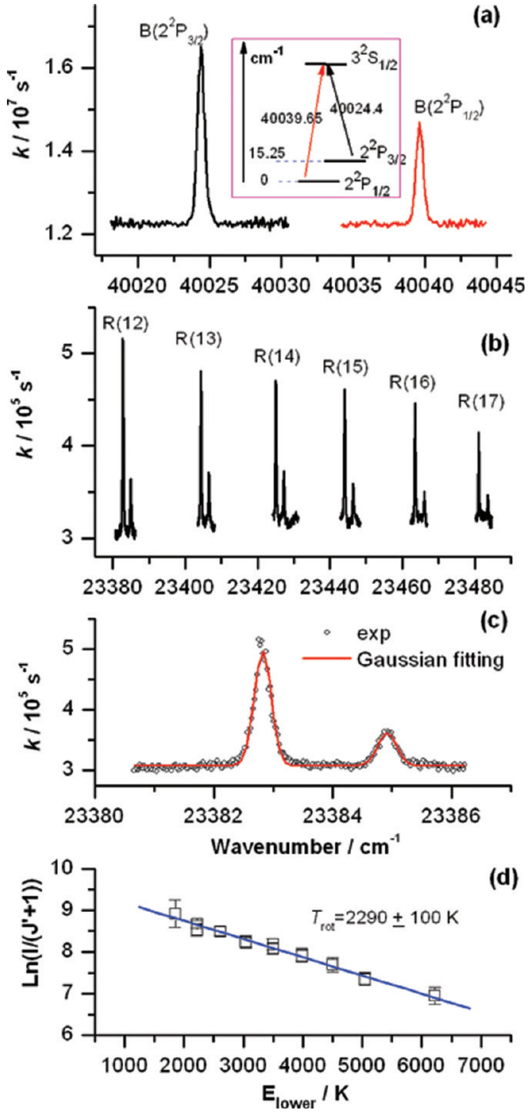

Figure 3. (a) CRD spectrum showing the two $B(3^2S \leftarrow {}^2P_J)$ lines of atomic B measured using $P = 1.5$ kW, $p = 150$ Torr, and $F(B_2H_6)$, F(Ar), and $F(H_2) = 0.003$, 40, and 525 sccm, respectively, along with a Grotrian diagram illustrating the relevant energy levels and transition wavenumbers. (b) CRD spectrum showing selected spectral lines from the R branch of the BH($A^1\Pi \leftarrow X^1\Sigma^+$) (0,0) band measured using conditions as in Figure 3a except that $F(B_2H_6) = 0.009$ sccm. (c) Expanded view of the R(12) line in Figure 3b, illustrating the extent to which the measured lines are described by Gaussian line shape functions. (d) BH rotational temperature determined from a Boltzmann plot of $\ln((I_{J'\leftarrow J''}/(J'+1))$ versus $E_{J''}$ derived from a spectrum obtained under conditions identical to those used in Figure 3b.

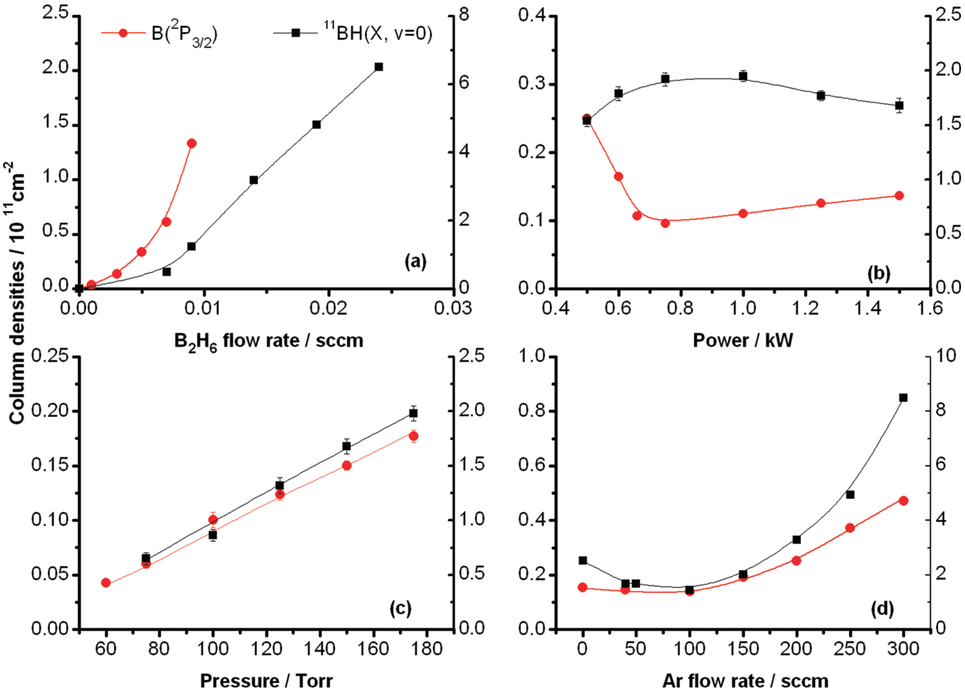

Figure 4. B($^2P_{3/2}$) and ^{11}BH(X, $v = 0$) column densities measured by CRDS (solid symbols, left- and right-hand vertical scales, respectively) plotted as a function of (a) $F(B_2H_6)$, (b) P, (c) p, and (d) F(Ar) with all other process parameters set at their base values. The B column densities displayed in panels b−d were each recorded using $F(B_2H_6) = 0.003$ sccm, whereas the BH column density measurements employed $F(B_2H_6) = 0.009$ sccm. The BH column densities have been calculated from the measured line-integrated absorbances of the R(14) line assuming $T_{rot} = 2300$ K.

PHER[44] with spectroscopic constants taken from ref 10) is shown in Figure 3d. The best-fit gradient returns a temperature of ~2300 K.

The B and BH column densities, {B} and {BH}, can be determined from the areas under the measured spectral lines. The column density of ^{11}BH (X, $v = 0$) radicals was determined as in our previous measurements of C_2(a) and CH(X) column densities in MW activated CH_4/H_2/Ar gas mixtures[25] using the equation

$$\{^{11}\mathrm{BH}(X, v = 0)\} = \frac{8\pi L\tilde{\nu}^2}{A_{00}p_T}\frac{g_{\mathrm{lower}}}{g_{\mathrm{upper}}}\int \Delta k \mathrm{d}\tilde{\nu} = \frac{4\pi L\tilde{\nu}^2}{A_{00}p_T}A_{\mathrm{spec}} \tag{2}$$

where $\tilde{\nu}$ is the wavenumber of the probe transition and $L = 84$ cm is the length of the cavity formed by the two CRDS mirrors. The Einstein A coefficient for the BH(A−X) (0,0) transition, $A_{00} = 7.86 \times 10^6$ s^{-1},[10] A_{spec} (in cm^{-1}), is the area covered by the spectral line, and p_T is a line-dependent weighting factor calculated with PGOPHER.[44] p_T is the calculated ratio of the integrated intensity of the spectral line under study to the total (0,0) band intensity (i.e., the sum of the integrated intensities of every rotational feature within the band) and is the only temperature-dependent parameter in eq 2. $p_T(T)$ values for the three BH lines used for the column density determinations reported here and in the companion paper[19] are listed in Table 3.

B column densities can be calculated in a similar manner using the expression

$$\{B_j\} = \frac{g_j}{g_k}\frac{8\pi L\tilde{\nu}_{jk}^2}{A_{kj}}\int \Delta k \, \mathrm{d}\tilde{\nu} = \frac{g_j}{g_k}\frac{8\pi L\tilde{\nu}_{jk}^2}{A_{kj}}A_{\mathrm{spec}} \tag{3}$$

where the j and k subscripts refer to, respectively, the lower ($2^2P_{1/2}$, $2^2P_{3/2}$) and upper ($3^2S_{1/2}$) levels in the transition, g_j and g_k are the respective degeneracies, $\tilde{\nu}_{jk}$ is the transition wavenumber, and A_{kj} is the Einstein coefficient for spontaneous emission, all of which are tabulated in the NIST Atomic Spectra Database.[45]

4.1.3. Variations in B and BH Column Densities with Discharge Parameters. Figure 4 shows the B($2^2P_{3/2}$) and ^{11}BH(X, $v = 0$) column densities measured at $z = 10$ mm as a function of $F(B_2H_6)$, P, p, and F(Ar). The B column densities in Figure 4b−d were each measured with $F(B_2H_6) = 0.003$ sccm, whereas $F(B_2H_6) = 0.009$ sccm was used for the BH column density measurements. The latter measurements employed the ^{11}BH(A−X), (0,0), R(14) line at 23 425.02 cm^{-1}. As Figure 3 shows, other lines (involving lower J'') are stronger

TABLE 3: PGOPHER Coefficients for Three BH(A−X) (0,0) Lines As a Function of Temperature in the Range 1500 < T < 3000 K

		$p_T(T)$				
transition	wavenumber/cm^{-1}	1500 K	2000 K	2300 K	2600 K	3000 K
R(14)	23 425.02	0.008632	0.011527	0.012544	0.013174	0.013588
R(11)	23 360.65	0.016467	0.017763	0.017781	0.017512	0.016916
R(10)	23 337.91	0.019384	0.019677	0.019235	0.018600	0.017633

under the present experimental conditions. Inspection of the p_T factors in Table 3 shows that the R(14) line offers a larger dynamic range than, for example, the R(10) line and enables measurement of higher column densities. Clearly, monitoring a yet higher J'' level would allow measurement of even higher column densities before saturation becomes an issue, but such lines have attendant disadvantages also. First, the associated absorbances may be too small to measure under low density conditions. Second, the associated p_T factors are increasingly sensitive to T_{rot}, and this temperature dependence must be accommodated when converting the measured column absorptions into ^{11}BH column densities. As Table 3 shows, the p_T factor for the R(14) line only varies by ~13% over the range 2000 K $\le T_{rot} \le$ 2600 K; for all {BH} determinations in this paper it is thus sufficient to assume T_{rot} = 2300 K.

As commented earlier (section 3.3) and illustrated by the OES measurements shown in section 4.2, the slow rate of surface passivation by B_yH_x species at low $F(B_2H_6)$ meant that it was necessary to wait (for >10 min) after each adjustment of $F(B_2H_6)$ before steady-state (or even near-steady-state) B and BH densities are attained. This provides one potential source of error in the present column density measurements. Another is the role of any trace air (O_2) impurity. As Figure 4a shows, {^{11}BH(X, v = 0)} shows a near linear dependence with $F(B_2H_6)$ once $F(B_2H_6) > 0.006$ sccm but appears to cutoff at $F(B_2H_6) < 0.006$ sccm. {B($2^2P_{3/2}$)} also shows a nonlinear dependence across the range 0.001 sccm $\le F(B_2H_6) \le$ 0.009 sccm. As discussed above, both of these latter trends at low $F(B_2H_6)$ are attributable to the influence of trace amounts of air impurity in the gas mixture. The detailed comparison of the calculated and experimental spatially-resolved {B($2^2P_{3/2}$)} and {^{11}BH(X, v = 0)} profiles is presented in Figure 5a and discussed below.

Figure 4b shows the measured P dependences of {B($2^2P_{3/2}$)} and {^{11}BH(X, v = 0)}. Increasing P from 0.5 to 0.75 kW results in a modest increase in {^{11}BH(X, v = 0)} but a sharp decrease in {B($^2P_{3/2}$)}; further increase in P causes a reversal of both trends. At this point we note that the B and BH column densities returned by the CRDS measurements require further scaling in order to derive the total B and BH column densities. In the case of atomic B, the displayed densities are for the ground ($2^2P_{3/2}$) spin–orbit state. As shown in Figure 3a, the small spin–orbit splitting ensures that this state and the spin–orbit excited ($2^2P_{1/2}$) state are populated in accord with their respective degeneracies and that $\{B\}_{total}$ = 1.5{B($^2P_{3/2}$)}. In the case of BH, the measured ^{11}BH column densities must be multiplied by a factor of 1.25 to accommodate the fraction of the total population associated with the minority ^{10}BH isotopologue, i.e., {BH(X, v = 0)}$_{total}$ = 1.25{^{11}BH(X, v = 0)}. Of course, {BH(X, v = 0)}$_{total}$ is still not the total BH column density. The wavenumber separation between the v = 0 and 1 levels of the ^{11}BH radical is 2269 cm^{-1}.[8] The ratio {BH(X, v = 1)}$_{total}$/{BH(X, v = 0)}$_{total}$ would be ~0.2–0.3 if the vibrational state population is equilibrated at the local gas temperatures T_{gas} along the column, so {BH(X)}$_{total}$ ≈ (1.56 ± 0.06){^{11}BH(X, v = 0)}$_{total}$.

Estimating $\{B\}_{total}/\{BH(X)\}_{total}$ for comparison with the model outputs is difficult given the nonlinear dependences of both column densities with $F(B_2H_6)$ at low $F(B_2H_6)$ but it is appropriate to describe trends in the ratio. In the case of P (Figure 4b), $\{B\}_{total}/\{BH(X)\}_{total}$ follows the trend in {B($2^2P_{3/2}$)}. The current modeling suggests that the BH and B densities are largely controlled by the fast H-shifting reaction R4, which is exothermic in the forward direction (Table 2). T_{gas} and [H] both increase with increasing P. As shown previously,[12] K_4 falls with increasing T_{gas}. On this basis, the $\{B\}_{total}/\{BH(X)\}_{total}$ ratio might be expected to decrease with increasing P. Increasing T_{gas} (by increasing P) also increases [H], however, which will drive R4 in the forward direction, consistent with the observed behaviors of {^{11}BH(X, v = 0)}, {B($2^2P_{3/2}$)}, and the $\{B\}_{total}/\{BH(X)\}_{total}$ ratio at P > 0.75 kW. The trends in B and BH column densities seen at P < 0.75 kW most probably reflect significant changes (and differences) in the T_{gas}, H, H_2O, HBO, B, and BH spatial distributions (and thus the measured column densities) as the size of the plasma ball shrinks dramatically at very low P. A detailed comparison of the spatially-resolved {B($2^2P_{3/2}$)} and {^{11}BH(X, v = 0)} profiles determined experimentally with those returned by the 2-D modeling will be presented in Figure 5b and discussed at that point.

Figure 4c shows that {^{11}BH(X, v = 0)} and {B($2^2P_{3/2}$)} both increase roughly linearly with p, as might be expected, given that the B_2H_6 number density in the source gas mixture scales with p, but the proportionality constant is not unity; doubling p results in a ~2.8-fold increase in {BH_x}. 2-D model calculations with $F(B_2H_6)$ = 0.009 sccm show a ~2-fold increase in {B_2H_6} upon increasing p from 75 to 150 Torr and a similar near 3-fold increase in {BH_x}, i.e., {^{11}BH(X, v = 0)} = 7.7 × 10^{10} cm^{-2}, {B($2^2P_{3/2}$)} = 2.15 × 10^{11} cm^{-2} at p = 75 Torr and {^{11}BH(X, v = 0)} = 2.2 × 10^{11} cm^{-2}, {B($2^2P_{3/2}$)} = 7.3 × 10^{11} cm^{-2} at p = 150 Torr. The more than proportionate growth of {BH_x} with p implies that one or more loss/production processes do not scale proportionately with p. The main processes within the reaction mechanism given in Table 1 are R1–R4 and R7 due, in particular, to the nonlinear dependences of both {H_2O} and {H} with p (i.e., {H_2O} ≈ 5.7 × 10^{12} cm^{-2} at z = 9.5 mm for both pressures, whereas {H} = 5.8 × 10^{16} cm^{-2} and 2 × 10^{17} cm^{-2} at z = 9.5 mm for p = 75 and 150 Torr, respectively) and the different gas temperature distributions (maximal gas temperatures ~2770 and ~2870 K for p = 75 and 150 Torr, respectively).

Figure 4d displays the observed trends in {B($2^2P_{3/2}$)} and {^{11}BH(X, v = 0)} as H_2 is progressively replaced by Ar. Increasing F(Ar) up to ~100 sccm (i.e., $F(Ar) \ll F(H_2)$ = 565–F(Ar)) has little effect on the plasma chemistry or parameters (T_{gas}, T_e, n_e) and thus little effect on {B} and {BH}. Further increases in F(Ar) (i.e., F(Ar) > 100 sccm), while maintaining the input power constant, leads to a reduction in the power density since less of the electron energy is expended on rotational and vibrational excitation of H_2.[24,46] Thus, the hot plasma volume expands. Intuitively, T_{gas} might have been expected to increase as a result of the declining thermal conductivity of the gas mixture with increasing F(Ar). As the present calculations show, however, this is compensated by the reduction in power density and the maximal gas temperature remains roughly constant. Studies of the rotational temperatures of $C_2(a)$ radicals in MW activated C/H/Ar plasmas as H_2 is progressively replaced by Ar (to the point that F(Ar) is ~80% of F_{total}) return broadly similar findings.[25,47] The observed increases in both {^{11}BH(X, v = 0)} and {B($2^2P_{3/2}$)} at F(Ar) >100 sccm can again be understood, qualitatively at least, in terms of the differing T_{gas} dependences of K_4. At progressively higher F(Ar), the hot plasma expansion becomes the dominant factor and the increase in both measured column densities can be attributed to the increased volume supporting effective thermal dissociation of B_2H_6.

4.1.4. Spatial Profiles. Figure 5 (filled symbols) shows the measured z dependences of {B($2^2P_{3/2}$)} and {^{11}BH(X, v = 0)} for input MW powers, P = 1.5 (Figure 5a) and 0.6 kW (Figure 5b). Again, $F(B_2H_6)$ = 0.003 and 0.009 sccm, respectively, when

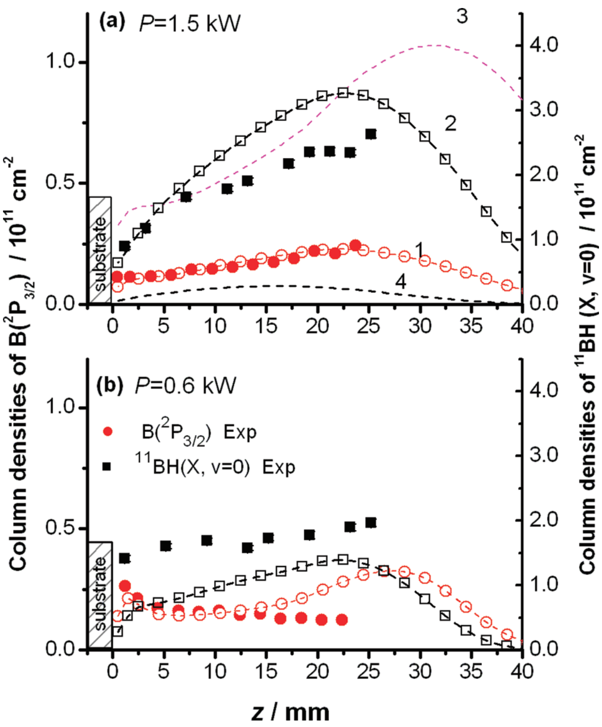

Figure 5. $B(^2P_{3/2})$ and $^{11}BH(X, v = 0)$ column densities measured by CRDS (filled symbols, left- and right-hand vertical scales, respectively), plotted as a function of z when P = (a) 1.5 and (b) 0.6 kW with all other process parameters set at their base values. The BH column densities were determined from the LIAs of the R(11) and R(10) lines (in Figure 5a and 5b, respectively) using $F(B_2H_6)$ = 0.009 sccm. $F(B_2H_6)$ = 0.003 sccm was used for the B density measurements. The open symbols linked by the dashed curves in Figure 5a (labeled 1 and 2) and 5b illustrate the corresponding z-dependent $\{B(2^2P_{3/2})\}$ and $\{^{11}BH(X, v = 0)\}$ values predicted (for the appropriate B_2H_6 flow rates) by the reactor modeling described in section 3.5. Note that the calculated $B(^2P_{3/2})$ column densities displayed in Figure 5a and 5b have been divided by, respectively, 4 and 3 for display purposes. For completeness, in Figure 5a, the dashed curves labeled 3 and 4 show the calculated $\{B(^2P_{3/2})\}$ value for $F(B_2H_6)$ = 0.009 sccm (after division by 15 for ease of display) and the $\{^{11}BH(X, v = 0)\}$ value calculated with 0.003 sccm.

sampling B and BH. The $\{^{11}BH(X, v = 0)\}$ were determined by monitoring the integrated absorbance of the R(11) line in the case that P = 1.5 kW, while the R(10) line was used in the P = 0.6 kW study. As Table 3 shows, the PGOPHER coefficients for both of these lines are relatively insensitive to T, and again, we assumed T_{rot} = 2300 K in deriving the column densities shown in this figure. Figure 5a also shows the absolute $\{B(2^2P_{3/2})\}$ and $\{^{11}BH(X, v = 0)\}$ profiles returned by the model calculations (open symbols) for $F(B_2H_6)$ = 0.003 and 0.009 sccm obtained by summing the calculated number densities from $-6 \leq r \leq +6$ cm for each z. The modeling reproduces the experimental trends well but overestimates the measured $B(2^2P_{3/2})$ column densities. Several possible contributory reasons for this discrepancy can be envisaged. For example, the model does not allow for possible variations in the T_e distribution within the plasma region. Other studies[48] have suggested that T_e declines by ∼10% with increasing distance from the substrate, however, which would have some effect on the H-atom distribution (as discussed elsewhere[24]) and thus the calculated {B} and {BH} profiles. Experimentally, the difficulty of attaining genuinely steady-state conditions could also contribute to the discrepancy between the measured and the calculated absolute {B} and {BH} values, especially at low $F(B_2H_6)$. For example, time-resolved studies (Figure 7, see later) show the B* emission intensity to still be increasing slowly ∼1 h after introducing $F(B_2H_6)$ = 0.003 sccm into a pre-existing Ar/H_2 plasma.

Three aspects of these data merit comment. First, the $\{B(2^2P_{3/2})\}$ and $\{^{11}BH(X, v = 0)\}$ profiles under base conditions (P = 1.5 kW) are very extensive; both are still increasing at $z > 20$ mm, in contrast to the C_2(a) and CH(X) radical column densities measured in MW activated $CH_4/H_2/Ar$ plasmas in this same reactor (which peak at $z \approx 10$ mm).[25] Both BH_x profiles and the magnitudes of $\{B(2^2P_{3/2})\}$ and $\{^{11}BH(X, v = 0)\}$ are reproduced well by the model calculations, with the biggest discrepancy the ∼4-fold overestimation of $\{B(2^2P_{3/2})\}$ at all z. Second, the $\{B\}_{total}/\{BH(X)\}_{total}$ ratio in both P regimes increases markedly on approaching the substrate where T_{gas} and [H] both drop sharply as $z \rightarrow 0$. The trend in the $\{B\}_{total}/\{BH(X)\}_{total}$ ratio can be understood if the decline in T_{gas} is the dominant effect, increasing K_4 and shifting $R4$ in favor of the products. Third, reducing P from 1.5 to 0.6 kW results in an increase in both column densities measured at small z. The $\{^{11}BH(X, v = 0)\}$ profile becomes flatter, while the $\{B(2^2P_{3/2})\}$ profile at P = 0.6 kW increases steeply as $z \rightarrow 0$. The substantial ∼3-fold reduction of plasma volume upon reducing P from 1.5 to 0.6 kW will affect the BH and B column densities (Figure 5b) in several ways as a result of changes in the gas temperature, the H, H_2O, and HBO concentrations, and their respective spatial distributions.

4.2. OES Measurements and Results. In contrast to the CRDS absorption measurements discussed above, OES involves radiation from excited species and is thus a more sensitive probe of changes in the electron properties of the plasma (i.e., n_e and T_e). As shown previously,[25,26] many additional insights can be obtained by comparing and contrasting results from OES and CRDS measurements.

4.2.1. 'Halo'. Addition of B_2H_6 to a pre-existing Ar/H_2 plasma leads to the appearance of a very obvious purple 'halo' around the central plasma ball. When using high $F(B_2H_6)$ or under high P conditions, the halo appears to fill the chamber and results in the accumulation of a brown-colored film on the top quartz window of the reactor. The intensity of the H Balmer emission from the plasma is seen to decline steadily with time once this film is forming (i.e., within ∼1 h after introducing $F(B_2H_6)$ = 0.025 sccm into an Ar/H_2 plasma under standard conditions), implying that progressively less MW power is coupling into the reactor. The purple halo is attributable to BH(A → X) emission. The appearance of the halo can be understood by recognizing that although n_e is quite low in the region outside the plasma ball, the BH density is sufficiently high and the BH(A ← X) excitation energy sufficiently low that enough BH radicals are excited by electron impact excitation to yield purple emission intensities that are visible by the eye. In the absence of B_2H_6, however, even though H_2, Ar, and even H (n = 1) atoms are present at high number density in the periphery of the Ar/H_2 plasma, the energy separations between the ground and the first excited states of these species are all too large to be excited by the electrons available in this region and no halo is observed.

4.2.2. Variation as Functions of Discharge Parameters. Figure 6 shows the BH, H_α, H_β, and H_2 emissions measured (through an optical fiber directed at the center of the plasma ball at $z \approx 10$ mm above the substrate surface) as a function of the same discharge parameters (P, p, $F(B_2H_6)$, and F(Ar)), normalized so that the maximum signal associated with each species is set to unity. BH is monitored via its A → X (0,0) Q branch at ∼433.2 nm, while the spectral features used for tracing the other three species have been detailed in ref 26.

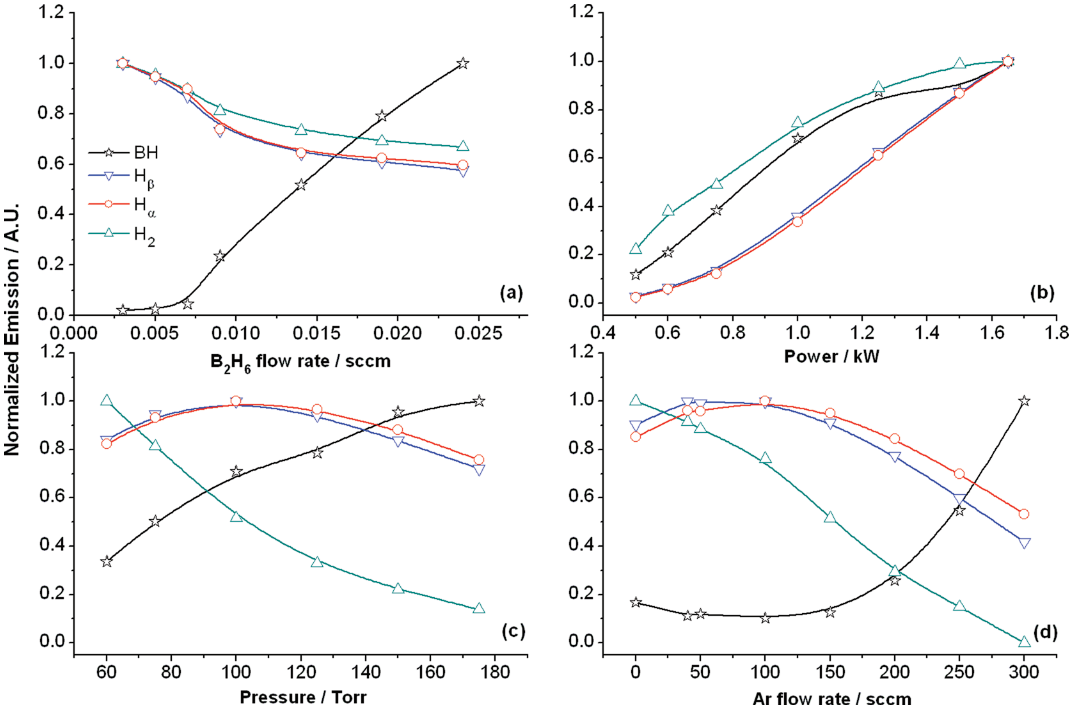

Figure 6. Optical emission intensities from BH, H$_\alpha$, H$_\beta$, and H$_2$ as a function of (a) $F(B_2H_6)$, (b) P, (c) p, and (d) $F(Ar)$ normalized so that for each emitter within a given plot the peak emission intensity is unity. All discharge parameters (apart from the one being varied) were held at their base values, apart from $F(H_2)$, which was adjusted to maintain $F_{total} = 565$ sccm when varying $F(Ar)$ away from its base value.

Figure 6a illustrates the ways in which the chosen emissions vary with $F(B_2H_6)$. The H$_\alpha$ and H$_\beta$ emissions behave very similarly, indicating that T_e is relatively insensitive to addition of trace quantities of B_2H_6, though the observation that the H$_\alpha$, H$_\beta$, and H$_2$* emission intensities all decline suggests that increasing $F(B_2H_6)$ does have some effect on T_e. As detailed previously, the 2-D model calculations also indicate some fall in T_e following the increase in plasma volume induced by B_2H_6 addition. The BH* emission shows a nonlinear dependence on $F(B_2H_6)$, which we attribute to the effects of trace amounts of air impurity, as discussed in sections 3.4 and 4.1.3. The calculated trends in BH, H ($n = 3$), and H$_2$* column densities all match the trends in the respective emissions well, i.e., $\{^{11}BH(X, v = 0)\} = 2.4 \times 10^{10}$ cm^{-2}, $\{H (n = 3)\} = 1.9 \times 10^7$ cm^{-2}, $\{H_2^*\} = 7.6 \times 10^9$ cm^{-2} at $F(B_2H_6) = 0.003$ sccm, cf. $\{^{11}BH(X, v = 0)\} = 2.2 \times 10^{11}$ cm^{-2}, $\{H (n = 3)\} = 1.4 \times 10^7$ cm^{-2}, $\{H_2^*\} = 6 \times 10^9$ cm^{-2} at $F(B_2H_6) = 0.009$ sccm.

As Figure 6b shows, all of the selected emissions increase with increasing P but those due to BH and H$_2$ increase less steeply than the H$_\alpha$ and H$_\beta$ emissions. We have already seen that the BH ground-state density (measured by CRDS, Figure 4b) decreases with power at $P > 0.75$ kW. The fact that the BH* emission is observed to increase with P can be explained by the associated increase in n_e. The H$_\alpha$ and H$_\beta$ emissions show identical trends, implying that T_e changes little upon increasing P.[26] Both increase more steeply than the H$_2$* emission, reflecting the fact that increasing P results in an increase of both H ($n = 1$) and n_e, whereas only the latter increase benefits the H$_2$* emission. Again, the calculated trends in BH, H ($n = 3$), and H$_2$* column densities all match well with the observed trends in the respective emission intensities, i.e., $\{^{11}BH(X, v = 0)\} = 9.5 \times 10^{10}$ cm^{-2}, $\{H (n = 3)\} = 4.1 \times 10^6$ cm^{-2}, $\{H_2^*\} = 6.2 \times 10^9$ cm^{-2} at $F(B_2H_6) = 0.009$ sccm, and $P = 600$ W, as compared with the base values ($P = 1500$ W) listed above.

The H$_\alpha$ and H$_\beta$ curves cross upon increasing p (Figure 6c), consistent with previous conclusions that T_e in these MW activated plasmas falls as p is raised.[26] (The present calculations return $T_e = 1.45$ and 1.23 eV for $F(B_2H_6) = 0.009$ sccm and total pressures of 75 and 150 Torr, respectively.) Such a drop in T_e is also implied by the obvious fall in H$_2$* emission, which also depends sensitively on the high-energy tail of the EEDF. As commented earlier, electron impact excitation of BH* emission is reliant on less energetic electrons, and the observation that the BH* emission grows steadily with increasing p accords with the earlier observation (Figure 4c) that $\{^{11}BH(X, v = 0)\}$ scales roughly linearly with p. Again, the calculated BH, H ($n = 3$), and H$_2$* column densities are broadly consistent with the experimentally observed trends in the respective emission intensities, i.e., $\{^{11}BH(X, v = 0)\} = 7.7 \times 10^{10}$ cm^{-2}, $\{H (n = 3)\} = 2 \times 10^7$ cm^{-2}, $\{H_2^*\} = 1.8 \times 10^{10}$ cm^{-2} at $p = 75$ Torr, cf. $\{^{11}BH(X, v = 0)\} = 2.2 \times 10^{11}$ cm^{-2}, $\{H (n = 3)\} = 1.4 \times 10^7$ cm^{-2}, $\{H_2^*\} = 6 \times 10^9$ cm^{-2} at $p = 150$ Torr.

Figure 6d shows how the various emissions are affected by the progressive replacement of H$_2$ by Ar. The H$_\alpha$ and H$_\beta$ emission curves cross, hinting at some reduction in T_e, and the intensities of the H$_\alpha$ and H$_\beta$ emissions at $F(Ar) = 300$ sccm are roughly one-half that under base conditions ($F(Ar) = 40$ sccm). As shown earlier (Figure 4d), substituting H$_2$ by Ar results in some expansion of the hot plasma region but has relatively little effect on the plasma parameters when $F(Ar) < 100$ sccm; the present data suggests that T_e, n_e, and the maximal T_{gas} remain relatively constant across the entire range 0 sccm $< F(Ar) < 300$ sccm. For example, the main source of H ($n = 1$) atoms is thermal dissociation of H$_2$. The observed ~2-fold reduction in the H$_\alpha$ and H$_\beta$ emissions upon increasing $F(Ar)$ to 300 sccm could thus be understood as simply mirroring the ~2-fold reduction in the partial pressure of H$_2$ and thus in the H ($n = 1$) concentration. At first glance, the order of magnitude drop in H$_2$* emission intensity upon increasing $F(Ar)$ from base conditions to 300 sccm (Figure 6d) might be attributed to a marked decline in T_e. None of the variations in p or $F(Ar)$ cause more than 2-fold change in the H$_\alpha$ and H$_\beta$ emissions however,

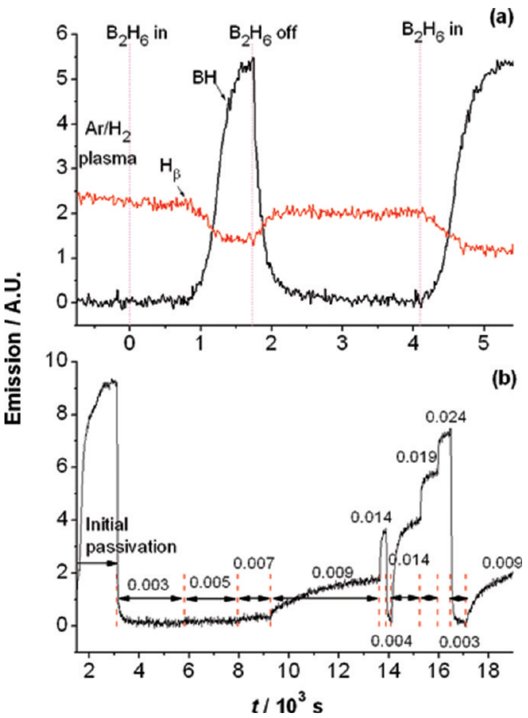

Figure 7. Temporal behavior of (a) BH* and $H_β$ emissions when $F(B_2H_6)$ in a $B_2H_6/Ar/H_2$ plasma is switched on and off. The B_2H_6 gas used in recording this data was a 5% mixture in H_2 and flowed at 0.5 sccm (i.e., $F(B_2H_6) = 0.025$ sccm) and (b) the BH* emission when $F(B_2H_6)$ in a $B_2H_6/Ar/H_2$ plasma was varied as indicated. The standard 200 ppm B_2H_6 in H_2 mixture was used in recording this latter data, $F(B_2H_6)$ was raised from 0 to 0.024 sccm at $t = 0$, and adjusted to the values shown above/below the trace at the times indicated by the vertical dashed lines.

suggesting that the H_2* emission intensity is a rather sensitive function of the argon concentration. Increasing p(Ar) pressure 16-fold while maintaining $p(H_2)$ at ~70 Torr causes the H_2* emission to drop by roughly 2 orders of magnitude. Such a decline is most likely an indication of H_2* quenching by and/or reactions with Ar, e.g., $H_2^* + Ar \rightarrow ArH^* + H$. The related reactive processes $Ar^* + H_2 \rightarrow ArH^* + H$ are known.[49] The trend in BH* emission with increasing F(Ar) is reminiscent of that shown in Figure 4d and, as before, is explicable in terms of the increased thermal dissociation of B_2H_6 as a result of the hot plasma expansion.

4.2.3. Passivation Effects. Figure 7 shows two data sets illustrating aspects of the temporal behavior of the BH* emissions when varying $F(B_2H_6)$ in an Ar/H_2 plasma. Figure 7a shows early data recorded using a slow (0.5 sccm) flow of a concentrated 5%B_2H_6 in H_2 mixture ($F(B_2H_6) \equiv 0.025$ sccm). The reactor in this case had been opened to air and then re-evacuated for several hours, prior to igniting an Ar/H_2 plasma. The B_2H_6 source gas was then switched on. The BH* emission intensity shows a 'dead' induction time, t_{ind}, of ~15 min and then increases during a period (t_{growth}) that endures for (at least) 10 min. Subsequent off/on cycles showed a similar slow build up of BH* intensity but not the induction period.

These observations can be rationalized as follows. The induction and growth times are orders of magnitude longer than the characteristic diffusional times (which are on the order of seconds). The absence of BH* emission at early time indicates that B_yH_x species are being destroyed en route to the hot plasma region. As discussed earlier (section 3), possible destruction mechanisms include (i) gas-phase loss reactions with H_xO_z or (ii) heterogeneous loss at the reactor walls. The former is an unlikely explanation for the observed induction period. $F(B_2H_6) = 0.025$ sccm corresponds to a B-atom flow rate of 2.22×10^{16} s^{-1}; thus, $\sim 2 \times 10^{19}$ B atoms must be destroyed during the induction period. This would require an improbably high average concentration of gas-phase H_xO_z species.

Process (ii) can be realized as follows, with $t = 0$ defining the time when $F(B_2H_6)$ is switched on. The reactivity of boron-containing species is widely recognized.[22] With a 'clean' reactor, we envisage fast loss/adsorption of B_yH_x species at the surfaces immediately downstream of the MFC (i.e., in the length of stainless steel gas line separating the MFC from the mixing manifold leading into the reactor, the reactor wall itself near the gas inlets and neighboring areas of the quartz window). B_yH_x species are assumed to react heterogeneously with surface-adsorbed H_xO_z species (possibly activated by gas-phase H or O atoms) or to be adsorbed at the surface (B-atom adsorption followed by reactions with H_2O and O_2, section 3.3) up to the point of saturation or until equilibrium between reaction and reverse etching processes has been attained, at which time the effective loss probability is assumed to decrease substantially. Possible sources for the surface H_xO_z species (e.g., OH groups, H_2O, etc.) include adsorption from air (when the reactor was not in operation), small vacuum leaks, trace air contamination in the input gas mixture, and possible outgassing from the reactor materials. The density of gas-phase B_2H_6 in the input regions of the reactor then starts to increase and diffuse further into the reactor volume, encountering new areas of 'clean' surface covered with adsorbed H_xO_z species.

Such sequential processing of (and heterogeneous loss to) the reactor surface provides an explanation for $t_{ind} \approx 15$ min before gas-phase B_2H_6 molecules reach the detection region ($z \approx 10$ mm) and yield the observed BH* emission. Once $t > 15$ min, surfaces further from the gas input lines (e.g., the base of the reactor and the side arms supporting the CRD mirrors) still remain to be passivated, and heterogeneous loss of B_2H_6 only ceases after a further time ($t_{growth} > 10$ min), once B_2H_6 and the various BH_x have come into steady state. The BH* emission falls to zero upon interrupting $F(B_2H_6)$ but over a long time scale ($t_{decay} \approx 400$ s), which can be understood if we assume some continued etching of the more reactive components within the $B_yH_xO_z$ adsorbate. After this time, the walls are deemed to be passivated with a $B_yH_xO_z$ coating which, while $F(B_2H_6) = 0$, progressively adsorbs a new H_xO_z surface layer. Upon reinstating $F(B_2H_6)$, therefore, we observe a repeat of the t_{growth} phase but without the t_{ind} period as the underlying reactor surface is already passivated with the $B_yH_xO_z$ coating.

Apart from illustrating this passivation effect, Figure 7a also reveals an anticorrelation between the BH* and $H_β$ emissions. B-containing species all have low ionization thresholds however.[9,50] Addition of even small amounts of B_2H_6 can thus cause some reduction of T_e and thus of $H_β$ and $H_α$, H_2*, and Ar* emissions, consistent with the data shown in Figure 6a.

Figure 7b shows the time evolution of the BH* emission intensities monitored while varying $F(B_2H_6)$ for the CRDS measurements of BH column densities shown in Figure 6a. The BH* emission observed with this more dilute, faster flowing gas supply exhibited a more complex time behavior during the initial passivation phase, but again, the BH* emission only appeared to reach steady state after ~30 min. Two other features of this plot are noteworthy. First, the >20-fold drop in BH* emission intensity upon reducing $F(B_2H_6)$ to 0.003 sccm (i.e., by a factor of 8). This is consistent with previous discussions of the disproportionate effect that traces of air impurity have at the lowest $F(B_2H_6)$, recall Figure 6a. Second, the time response

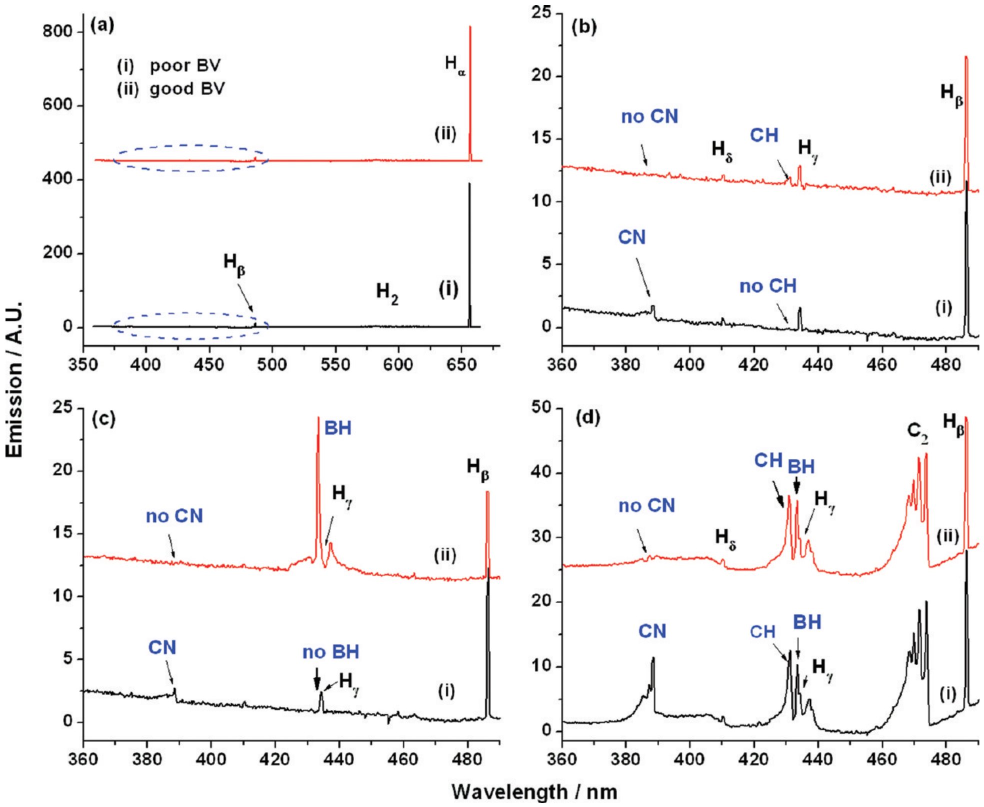

Figure 8. Optical emission spectra from (a) an Ar/H_2 plasma operating under (i) poor and (ii) good base vacuum (BV) conditions, (b) the same two plasmas, expanding the highlighted region to illustrate the presence of weak CN* emission under the poorer BV conditions, (c) the same two Ar/H_2 plasmas 30 min after introducing $F(B_2H_6) = 0.025$ sccm, and (d) the two B_2H_6/Ar/H_2 plasmas in Figure 8c 1 min after adding $F(CH_4) = 25$ sccm.

of the BH* emission intensity is clearly faster when reducing $F(B_2H_6)$ than when increasing it. This, too, is consistent with the foregoing discussion wherein it is assumed that gas-phase BH_x species only reach their asymptotic densities once the heterogeneous (wall) loss processes have come into steady state.

4.2.4. Effects of Traces of Air Impurity. We proposed that the nonlinear dependences of the B and BH column densities and emission intensities at low $F(B_2H_6)$ (recall Figures 4a and 6a) are attributable to trace air contamination. Figure 8 provides more direct evidence of such effects. Panels a and b show OE spectra measured under the same discharge conditions but with different base vacuums (BV). The ‘good’ base vacuum is limited by the rotary pump used to evacuate the reactor, a few mTorr, as reported by a Pirani gauge. Under normal operation, the reactor volume is flushed by process gas, each constituent of which has stated impurity levels < 100 ppm. The alternative data was recorded with a poorer vacuum, ~20 mTorr worse than the good vacuum, caused by a small leak where the quartz window sealed in the top of the reactor. As we now show, an air impurity of this magnitude (20 mTorr of air equates to an O_2 mole fraction of ~27 ppm under base conditions) can have a profound influence on the emission characteristics of a B_2H_6/Ar/H_2 plasma.

At first glance, the two OE spectra from the Ar/H_2 plasmas operating with different BV (Figure 8a) appear identical. As Figure 8b shows, however, more careful scrutiny of an exploded view of the region highlighted in panel a reveals weak CN(B → X) emission at ~388 nm,[51] a tell-tale signature of the presence of air impurity in H/C discharges, but only in the case of the poorer BV. The OE spectrum recorded with the good BV also shows one distinctive feature, a weak CH(A → X) emission at ~431 nm, attributable to etching of some carbon contaminant on the substrate surface. Figure 8c shows the corresponding spectra recorded 30 min after introducing $F(B_2H_6) = 0.025$ sccm into these Ar/H_2 plasmas. BH(A → X) emission is clearly evident in the plasma operating with the good BV, but no such emission is discernible from the plasma operating with the poorer BV, even 60 min after introducing $F(B_2H_6) = 0.025$ sccm. Again, this observation is consistent with the earlier discussion of the two different regimes for $BH_x + H_2O$ conversion to HBO. $F(B_2H_6) < F(O_2)$ under poor BV conditions and the presence of excess H_2O ensures efficient consumption of BH_x species via reactions *R*7 and *R*10. These trends should be contrasted with those observed when CH_4 is added to pre-existing B_2H_6/Ar/H_2 plasmas operating under either good or poor BV conditions. In both cases, strong BH* emission is immediately evident, reflecting the efficient gettering of H_2O (by conversion to CO) in the presence of excess hydrocarbon. As Figure 8d shows, the OE spectra of the B_2H_6/Ar/H_2 plasmas recorded 1 min after introducing $F(CH_4) = 25$ sccm look identical, apart for the persistent CN* emission from the plasma operating under poorer BV conditions. Such observations, which are wholly repeatable, provide further indication that air/O_2 initiates chemistry in B/H/Ar plasmas that leads to removal of BH_x species from the gas phase. One can envisage several factors that could account for the observation that addition of excess CH_4 getters the O_2 impurity. The presence of hydrocarbon will reduce the O (and H) atom densities near the reactor walls and, inevitably, alter the surface passivation processes, as will be discussed in the companion paper.[19] It will also reduce the density of gas-phase H_2O, with which B and, particularly, BH are known to react efficiently.[22,23] Given the rapidity of the

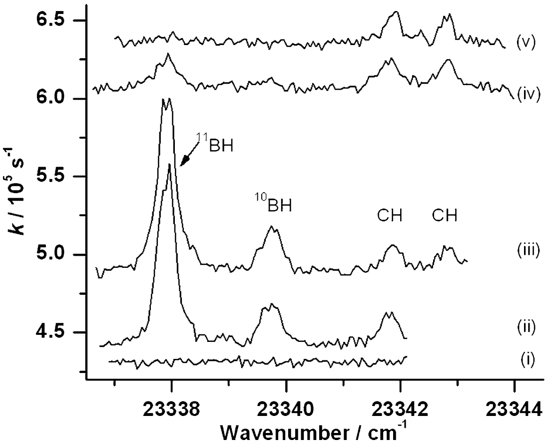

Figure 9. Time-resolved CRDS studies of the effect of adding $F(CH_4) = 25$ sccm to a pre-existing $B_2H_6/Ar/H_2$ plasma operating under base conditions but with the poorer BV: (i) 55 min after adding B_2H_6 to Ar/H_2 plasma, no BH absorption is observable; (ii) 1 min after adding CH_4 to the $B_2H_6/Ar/H_2$ plasma in (i), BH and CH are both observable; (iii) 3 min after the CH_4 addition in (ii), no further changes to the BH and CH column densities are evident; (iv) 1 min after switching off the B_2H_6 flow, (v) 3 min after switching off $F(B_2H_6)$, the BH absorptions disappear while those due to CH persist.

change in BH* emission upon adding CH_4, the latter is likely to be the most important factor under the prevailing experimental conditions.

Additional support for this view comes from CRDS studies of the effects of adding $F(CH_4)$ to a pre-existing $B_2H_6/Ar/H_2$ plasma operating under poor BV conditions. Figure 9 shows five absorption spectra measured across a 7 cm^{-1} range that allows monitoring of ground-state BH and CH radicals. Trace (i) in Figure 9 shows no discernible BH absorption 55 min after adding $F(B_2H_6) = 0.025$ sccm to a pre-existing Ar/H_2 plasma, a finding that accords with the OES data shown in Figure 8c. Introducing $F(CH_4) = 25$ sccm into this same $B_2H_6/Ar/H_2$ plasma causes an immediate build up of BH and CH column density within 1 min (trace (ii)). Neither absorbance evolves further (trace (iii) was measured 3 min after introducing $F(CH_4)$), indicating that $\{BH\}$ reaches its steady-state equilibrium value within 1 min of adding CH_4 to the plasma. $F(B_2H_6)$ was then switched to 0. As trace (iv) shows, the BH absorption is greatly reduced after 1 min but the CH absorbance is unchanged. After 3 min (trace (v)), the BH signals have fallen below the detection limit. These time-dependent measurements reinforce the conclusions reached through the OES studies, namely, that the presence of CH_4 greatly reduces the time it takes for the BH column density to reach its steady-state value in B/H/Ar-containing plasmas operating in the presence of traces of air contamination.

4.3. Studies of Material Deposited on the Reactor Walls.

Several ~1 cm^2 samples of aluminum wafer were attached to the inside walls at different locations within the reactor in order to investigate heterogeneous loss of boron from the $B_2H_6/Ar/H_2$ plasma. Figure 10 shows scanning electron microscope (SEM, JEOL JSM 5600LV) images of material deposited at the side wall while running the base B/Ar/H plasma at $P = 1$ kW for 6 h. This region would have remained close to 300 K throughout deposition. The low-resolution image in Figure 10a includes a TEM grid, which was attached to the wafer before it was introduced into the reactor with a view to estimating the deposit thickness and thus the rate of material deposition. Clearly, however, the deposited material is fibrous, as shown in the progressively higher resolution images in Figure 10b and 10c. Consequently, it was not possible to estimate a reliable deposition rate, but the deposit very clearly has a high surface to volume ratio. Material deposited on the reactor walls was also analyzed by mass spectrometry (using a MALDI-TOF instrument (Applied Biosystems 4700) and by traditional electron impact ionization (VG Analytical Autospec)). Mass peaks involving B, O, H, and Al (e.g., at m/z 89 and 90 $[AlB(OH)_3^+]$, at 105 and 106 $[AlOB(OH)_3^+]$, etc.) were clearly discernible, though no mass peaks associated with ions containing more than one B atom were identified. These analyses confirm that some of the boron introduced into the reactor is lost to the walls and that the solid deposit contains both H and O, in accord with previous discussions of likely wall loss mechanisms in gas-phase B/H/O chemistry.[22,23]

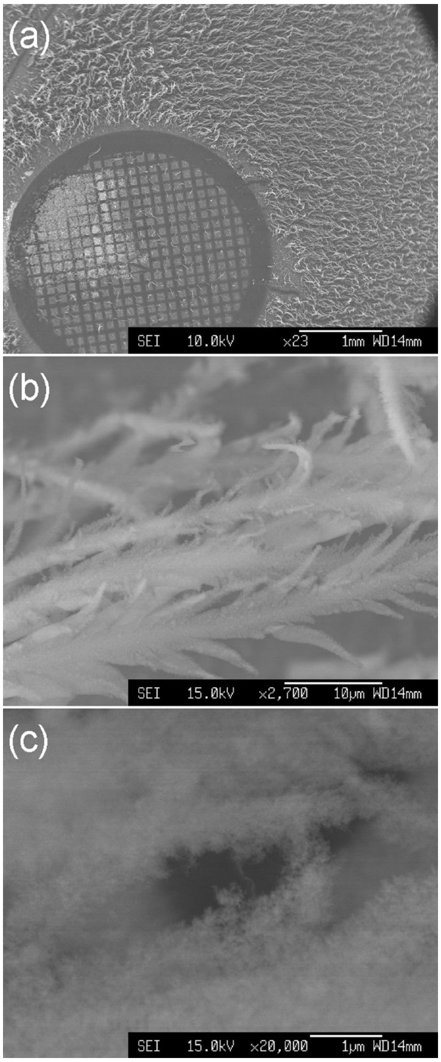

Figure 10. SEM images of the fibrous nanostructured deposit grown on an Al substrate mounted on the side wall of the reactor wall while discharging the base $B_2H_6/Ar/H_2$ gas mixture at $P = 1$ kW for 6 h. The respective length bars indicate (a) 1 mm, (b) 10 μm, and (c) 1 μm.

Only gas–surface reactions with low or zero activation barriers, E_a, can contribute to heterogeneous loss of boron at the low (~300 K) temperatures prevailing at the reactor walls. Information on such reactions is sparse, but known gas-phase reactions[40,52] can guide our thinking. As mentioned in section 3.4, the B + H_2O reaction results in several product channels,[40] in particular

$$\mathrm{B + H_2O \rightarrow HBO + H} \quad E_a \approx 32\ \mathrm{kJ\ mol^{-1}}$$

$$\mathrm{B + H_2O \rightarrow BOH + H} \quad E_a \approx 26\ \mathrm{kJ\ mol^{-1}}$$

The quoted activation barriers, from Chin et al.,[40] are likely to be overestimates given the reported rate coefficient for the B + H_2O reaction ($k_7 = 4.7 \times 10^{-12}$ cm^3 s^{-1}, ref 53), which accords with the value $E_a \approx 11.2$ kJ mol^{-1} assumed in Table 1. Gas-phase BOH is the less stable isomeric form of the product: $\Delta_f H$ (BOH) = -53 kJ mol^{-1} vs $\Delta_f H$ (HBO) = -239 kJ mol^{-1}.[40] With surface-adsorbed H_2O, however, the latter reaction appears more likely and, in the case of the aluminum side walls, could result in formation of AlBOH or AlOBOH species, for example. Exothermic gas–surface reactions such as

$$\mathrm{AlB + H_2O \rightarrow AlBOH + H}$$

and/or

$$\mathrm{AlBOH + H_2O \rightarrow AlB(OH)_2 + H}$$

may also be feasible following B-atom adsorption on an Al (or AlO) site, both of which yield H atoms that could return to the gas phase directly or following recombination with an adjacent surface-bound H or OH group or remain adsorbed at the surface.[54] Evidence supporting the feasibility of such mechanisms is provided by experimental studies of H_2O adsorption on a Rh surface.[55] Small amounts of boron segregated on the Rh surface resulted in much enhanced adsorption probabilities and dissociation of H_2O, as revealed by H_2 formation and the build up of B–O surface species.

5. Conclusions

The real and potential applications of B-doped CVD diamond are becoming recognized ever more widely. This paper reports a thorough investigation of MW activated dilute B_2H_6/Ar/H_2 plasmas which provides the necessary background to a subsequent study of the B_2H_6/CH_4/Ar/H_2 plasmas used for growth of B-doped CVD diamond.[19] The present investigation has involved (i) spatially resolved CRDS measurements of the absolute column densities of B atoms and BH radicals as a function of $F(B_2H_6)$, F(Ar), p, and P, (ii) OES measurements of the relative densities of electronically excited BH radicals, H atoms, and H_2 molecules as a function of the same process conditions and as a function of time after introducing B_2H_6 into a pre-existing Ar/H_2 plasma, and (iii) complementary 2-D(r, z) modeling of the plasma chemistry that includes due allowance for variations in the plasma parameters and conditions (e.g., T_e, T_{gas}, n_e, Q, and the plasma chemistry) as a function of the same process conditions. Comparisons between experiment and model outputs allow refinements to the existing B/H and B/H/O chemistry and thermochemistry and illustrate the progressive conversion of B_2H_6 to BH_3 to smaller BH_x species and (in the presence of O_2) to the more stable HBO species. Such comparisons also indicate that the monitored B and BH densities maximize outside the hottest central region of the plasma ball and extend over much larger regions of r, z space than, for example, the C_2 and CH radicals probed in previous studies of CH_4/Ar/H_2 plasmas operating at the same p and P in this same reactor.[25] Measured variations in the B and BH densities at low $F(B_2H_6)$ and time-dependent studies of the BH OES signal upon adding B_2H_6 to a pre-existing Ar/H_2 plasma serve to highlight significant loss of gas-phase BH_x density which, the modeling shows, can include contributions from both homogeneous (reaction with unintentional trace quantities of air/O_2 in the process gas mixture resulting in BH_x conversion into more stable $H_xB_yO_z$ species like HBO) and heterogeneous (adsorption of BH_x (mainly B atoms) and reaction at the reactor wall) mechanisms. The present study provides further illustration of the ways in which a combination of experiment and modeling, applied to a particular plasma science issue, can result in a whole that is substantially greater that the sum of the individual parts.

Acknowledgment. The Bristol group is grateful to EPSRC for funding, including the portfolio grant (LASER), to Element Six Ltd. for financial support and the long-term loan of the MW reactor, to the University of Bristol and the Overseas Research Scholarship (ORS) scheme for a postgraduate scholarship (J.M.), to colleagues K. N. Rosser and Drs. J. A. Smith and D. W. Comerford for their many contributions to the experimental work described here, and to Professor J. N. Harvey, and Drs. P. D. Gates and G. M. Fuge for help with, respectively, the ab initio quantum chemistry calculations and the mass spectroscopy and electron microscopy measurements. The Bristol-Moscow collaboration is supported by a Royal Society Joint Project Grant, and Y.A.M. acknowledges support from RF Government for Key Science Schools grant No. 133.2008.2.

References and Notes

(1) Kalish, R. *Carbon* **1999**, *37*, 781.

(2) Deneuville, A. *Semicond. Semimet.* **2003**, *76*, 183, and references therein.

(3) Collins, A. T.; Williams, A. W. S. *J. Phys. C: Solid State Phys.* **1971**, *4*, 1789.

(4) Hartmann, P.; Bohr, S.; Haubner, R.; Lux, B.; Wurzinger, P.; Griesser, M.; Bergmaier, A.; Dollinger, G.; Sternschulte, H.; Sauer, R. *Int. J. Refract. Met. Hard Mater.* **1997**, *16*, 223.

(5) Gheeraert, E.; Deneuville, A.; Mambou, J. *Carbon* **1999**, *37*, 107.

(6) Lee, B. J.; Ahn, B. T.; Baik, Y. J. *Diamond Relat. Mater.* **1999**, *8*, 251.

(7) Ramamurti, R.; Becker, M.; Schuelke, T.; Grotjohn, T.; Reinhard, D.; Asmussen, J. *Diamond Relat. Mater.* **2008**, *17*, 1320.

(8) Osiac, M.; Lavrov, B. P.; Röpcke, J. *J. Quant. Spectrosc. Radiat. Transfer* **2002**, *74*, 471.

(9) Lavrov, B. P.; Osiac, M.; Pipa, A. V.; Röpcke, J. *Plasma Sources Sci. Technol.* **2003**, *12*, 576.

(10) Rayar, M.; Veis, P.; Foissac, C.; Supiot, P.; Gicquel, A. *J. Phys. D: Appl. Phys.* **2006**, *39*, 2151.

(11) Comerford, D. W.; Cheesman, A.; Carpenter, T. P. F.; Davies, D. M. E.; Fox, N. A.; Sage, R. S.; Smith, J. A.; Ashfold, M. N. R.; Mankelevich, Y. A. *J. Phys. Chem. A* **2006**, *110*, 2868.

(12) Rayar, M.; Supiot, P.; Veis, P.; Gicquel, A. *J. Appl. Phys.* **2008**, *104*, 033304.

(13) Kohn E.; Denisenko, A. In *CVD Diamond for Electronic Devices and Sensors*; Sussmann, R. S., Ed.; John Wiley and Sons: New York, 2009; Chapter 14.

(14) Ekimov, E. A.; Sidorov, V. A.; Bauer, E. D.; Mel'nik, N. N.; Curro, N. J.; Thompson, J. D.; Stishov, S. M. *Nature* **2004**, *428*, 542.

(15) Sidorov, V. A.; Ekimov, E. A.; Stishov, S. M.; Bauer, E. D.; Thompson, J. D. *Phys. Rev. B* **2005**, *71*, 060502.

(16) Takano, Y. *J. Phys.: Condens. Matter* **2009**, *21*, 253201.

(17) Nebel, C. E.; Rezek, B.; Shin, D.; Uetsuka, H.; Yang, N. *J. Phys. D: Appl. Phys.* **2007**, *40*, 6443.

(18) Nebel, C. E.; Shin, D. C.; Rezek, B.; Tokuda, N.; Uetsuka, H.; Watanabe, H. *J. R. Soc. Interface* **2007**, *4*, 439.

(19) Ma, J.; Richley, J. C.; Davies, D. R. W.; Ashfold M. N. R.; Mankelevich, Y. Manuscript in preparation.

(20) Ruan, J.; Kobashi, K.; Choyke, W. J. *Appl. Phys. Lett.* **1992**, *60*, 1884.

(21) Sakaguchi, I.; Nishitani-Gamo, M.; Loh, K. P.; Yamamoto, K.; Haneda, H.; Ando, T. *Diamond Relat. Mater.* **1998**, *7*, 1144.

(22) Gal, G.; Bar-Ziv, E. *Int. J. Chem. Kin.* **1995**, *27*, 235.

(23) Bauer, S. H. *Chem. Rev.* **1996**, *96*, 1907, and references therein.

(24) Mankelevich, Y. A.; Ashfold, M. N. R.; Ma, J. *J. Appl. Phys.* **2008**, *104*, 113304.

(25) Ma, J.; Richley, J. C.; Ashfold, M. N. R.; Mankelevich, Y. A. *J. Appl. Phys.* **2008**, *104*, 103305.

(26) Ma, J.; Ashfold, M. N. R.; Mankelevich, Y. A. *J. Appl. Phys.* **2009**, *105*, 043302.

(27) Ma, J.; Cheesman, A.; Ashfold, M. N. R.; Hay, K. G.; Wright, S.; Langford, N.; Duxbury, G.; Mankelevich, Y. A. *J. Appl. Phys.* **2009**, *106*, 033305.

(28) Cheesman, A.; Smith, J. A.; Ashfold, M. N. R.; Langford, N.; Wright, S.; Duxbury, G. *J. Phys. Chem. A* **2006**, *110*, 2821.

(29) In *Handbook of Thermodynamic Properties of Individual Species*; Glushko V. P. , Eds.; Nauka: Moscow, 1981; Vol. XVIII, Book 2 (in Russian).

(30) *NIST-JANAF Thermochemical Tables*, 4th ed.; Chase, M. W., Jr., Ed.;*J. Phys. Chem. Ref. Data*, Monograph 9, 1998.

(31) Yu, C.-L.; Bauer, S. H. *J. Phys. Chem. Ref. Data* **1998**, *27*, 807.

(32) Values obtained using the XIV Reaction data facility of http://cccbdb.nist.gov.

(33) Sato, K.; Kanda, N.; Ogata, T.; Kumashiro, Y. *Chem. Phys. Lett.* **2000**, *325*, 453.

(34) Schlegel, H. B.; Baboul, A. G.; Harris, S. J. *J. Phys. Chem.* **1996**, *100*, 9774.

(35) Clarke, R. P.; Pease, R. N. *J. Am. Chem. Soc.* **1951**, *73*, 2132.

(36) Greenwood, N. N.; Greatrex, R. *Pure Appl. Chem.,* **1987**, *59*, 857, and references therein.

(37) Casadesus, P.; Frantz, C.; Gantois, M. *Metallurg. Trans. A* **1979**, *10A*, 1739.

(38) Smith, G. P.; Golden, D. M.; Frenklach, M.; Moriarty, N. W.; Eiteneer, B.; Goldenberg, M.; Bowman, C. T.; Hanson, R. K.; Song, C.; Gardiner, W. C., Jr.; Lissianski, V. V.; Qin, Z. http://www.me.berkeley.edu/gri—mech/.

(39) Sakai, S.; Jordan, K. D. *J. Phys. Chem.* **1987**, *83*, 2293.

(40) Chin, C.-H.; Mebel, A. M.; Hwang, D.-Y. *J. Phys. Chem. A* **2004**, *108*, 473.

(41) Yetter, R. A.; Rabitz, H.; Dryer, F. L. *Combust. Flame* **1991**, *83*, 43.

(42) Pasternack, L. *Combust. Flame* **1992**, *90*, 259.

(43) Ma, J. Ph.D. Thesis, University of Bristol, 2007.

(44) Western, C. M. PGOPHER, a Program for Simulating Rotational Structure; University of Bristol, http://pgopher.chm.bris.ac.uk.

(45) Ralchenko, Yu.; Kramida, A. E.; Reader J.; and NIST ASD Team. *NIST Atomic Spectra Database*, version 3.1.5; National Institute of Standards and Technology: Gaithersburg, MD, 2008; http://physics.nist.gov/asd3.

(46) Fox, O. J. L.; Ma, J.; May, P. W.; Ashfold, M. N. R.; Mankelevich, Y.A. *Diamond Relat. Mater.* **2009**, *18*, 750.

(47) Richley, J. C.; Fox, O. J. L.; Ashfold, M. N. R.; Mankelevich, Y. A. Unpublished results.

(48) Hassouni, K.; Grotjohn, T. A.; Gicquel, A. *J. Appl. Phys.* **1999**, *86*, 134.

(49) Gordillo-Vazquez, F. J.; Albella, J. M. *Plasma Sources Sci. Technol.* **2004**, *13*, 50.

(50) Basner, R.; Schmidt, M.; Becker, K. *J. Chem. Phys.* **2003**, *118*, 2153.

(51) Seo, H.; Kim, J.-H.; Chung, K.-H. *J. Appl. Phys.* **2005**, *98*, 043308.

(52) Garland, N. L.; Stanton, C. T.; Nelson, H. H. *J. Chem. Phys.* **1991**, *95*, 2511.

(53) DiGiuseppe, T. G.; Estes, R.; Davidovits, P. *J. Phys. Chem.* **1982**, *86*, 260.

(54) Brown, R. C.; Kolb, C. E.; Cho, S. Y.; Yetter, R. A.; Dryer, F. L.; Rabitz, H. *Int. J. Chem. Kinet.* **1994**, *26*, 319.

(55) Kiss, J.; Solymosi, F. *Surf. Sci.* **1986**, *177*, 191.

JP9094694